RICE UNIVERSITY

SWIR Imaging and Echelle Spectroscopy via Compressive Sensing

by

Lina Xu

A THESIS SUBMITTED
IN PARTIAL FULFILLMENT OF THE
REQUIREMENTS FOR THE DEGREE

Master of Science

APPROVED, THESIS COMMITTEE:

Kevin F. Kelly, Chairman
Associate Professor of Electrical and Computer Engineering

Frank K. Tittel
Professor of Electrical and Computer Engineering

Wotao Yin
Assistant Professor of Computational and Applied Mathematics

Houston, Texas
November, 2011

ABSTRACT

SWIR Imaging and Echelle Spectroscopy via Compressive Sensing

by

Lina Xu

A new sampling theory, called compressive sensing (CS), has recently emerged and its fundamental idea can be distilled as: it is possible to obtain near complete recovery of a signal/image from a small set of mixed measurements of it if the signal/image possesses properties akin to sparseness. Based on this theory, we have developed a unique hardware platform for imaging and spectroscopy applications which incorporates a spatial modulator and a single pixel detector. Random projections of the signal/image are applied to the light modulator and the modulated light is focused on the single detector generating a series of photovoltage values which are later used in the image reconstruction. For wavelengths outside the visible spectrum, where it is especially expensive to produce the large detector arrays, this scheme provides a far better solution using a single detector element.

ACKNOLEDGEMENTS

It is a great pleasure to thank many people who made this thesis possible.

Foremost, I would like to give my deepest appreciation to my advisor Dr. Kevin Kelly for his continuous support of my study and research, for his patience, motivation, enthusiasm, and immense knowledge. His guidance helped me in all the time of research and writing of this thesis.

Besides my advisor, I also want to express my gratitude towards our collaborators in Dr. Richard Baraniuk's group for their insightful comments and valuable support.

My sincere thanks also go to my fellow group members for their valuable discussions, emotional support, and their help to let me get through many difficulties.

Contents

List of Figures

Chapter 1

Introduction

This chapter aims to provide you with a big picture about compressive sensing (CS). Chapter 2 will elaborate on the detailed CS theory.

1.1 A Compressive Sensing Game: Sudoku Puzzle

Sudoku, a popular logic-based combinational number-placement puzzle is an ideal example where CS strategies can be employed in a gaming environment. The puzzle is traditionally solved by hand for fun, but various computer algorithms have been developed to solve these puzzles [1, 2]. Invented in the late 19th century, the objective of the puzzle is to fill a 9×9 grid with digits based on the constraints that each column, each row and each of the nine 3×3 sub-grids that compose the grid contain all the digits from 1 to 9. The initial occupied cells are called "clues" of the puzzles. Although the setter only provides a partially completed grid, each puzzle has only one solution by inserting a unique number in the particular position.

An example of an initial puzzle and its solution are shown in Figure 1.1.

To carry the analogy from a logic puzzle to an imaging theory, imagine the two dimensional array as an image instead of just a set of numbers. Although the image is sparse (there are missing data/pixels in the figure), there is only one result that can occur from properly interpreting this sample set. In other words, if we have prior information

about the structure of the image, sparseness in this case, we can extrapolate the image when there is only limited amount of available data just as we solve the puzzle.

5	3			7				
6			1	9	5			
	9	8					6	
8				6				3
4			8		3			1
7				2				6
	6					2	8	
			4	1	9			5
				8			7	9

5	**3**	4	6	**7**	8	9	1	2
6	7	2	**1**	**9**	**5**	3	4	8
1	**9**	**8**	3	4	2	5	**6**	7
8	5	9	7	**6**	1	4	2	**3**
4	2	6	**8**	5	**3**	7	9	**1**
7	1	3	9	**2**	4	8	5	**6**
9	**6**	1	5	3	7	**2**	**8**	4
2	8	7	**4**	**1**	**9**	6	3	**5**
3	4	5	2	**8**	6	1	**7**	**9**

Figure 1.1 A Sudoku Puzzle (left) and its solution with the unique filled numbers marked in red (right)

1.2 Rice Single-pixel Camera: What Makes It Possible?

Without any knowledge of CS, one could hardly imagine that an imaging system with only one detector element could, without scanning and measuring each pixel, produce a good quality high resolution image.

If one desired a 1 megapixel (MP) image, what would be the best course of action? The most direct way is to take the picture using a digital camera which has a one million pixel array of photo-detectors working together to record images as a series of points called pixels. The light values are converted into a huge set of numbers. These numbers are usually then compressed using methods such as JPEG, JPEG2000, MPEG etc. For example, JPEG compression performs a discrete cosine transform on this set of numbers and more than 90% of the transformed coefficients, which are zeroes or close to zeroes,

are discarded. The inherent inefficiency problem with "acquire first and compress later" scheme leads us to the question, "Why would one still take 100% of the measurement when we only need a few key ones to generate an image?"

To get the same 1 MP resolution with a single element detector, one can employ a raster scanning scheme. However, this requires the collection of 1 million serial measurements first and then assembling them to get the 1MP image, which is among other things, very time consuming.

Unlike the two schemes above, in the Rice single-pixel sensing system, an image of the scene is collected and projected by a lens onto a digital micromirror device (DMD) [3], fabricated by Texas Instruments. DMDs are primarily used in digital televisions and projector systems to digitally modulate emitted light. Each DMD consists of hundreds of thousands of micromirrors whose orientation can be precisely controlled to tilt either +12 degree or -12 degree about its diagonal. This switching function is controlled by a computer and directly corresponds to the elements of a binary matrix. Light from the scene falls on a Boolean white noise pattern and is split into one of two paths. Either of both paths can be focused by a second lens onto a photodiode which converts the light signal to photovoltage. Each time the mirrors shift, a new photovoltage value will be generated by the photodiode and recorded along with the mirror configuration which produced it. The original image is then reconstructed from this series of photovoltage values, by using certain nonlinear optimization algorithms. In comparison to the one million serial measurements required in scanning mode the single pixel camera is significantly more efficient. A detailed introduction to the single-pixel imaging system will be provided in chapter 3.

The overall design of this single pixel imaging system was inspired from CS theory which states that it is possible to reconstruct images or signals of interests accurately from a set of samples far smaller than the desired resolution of the image/signal if the signal meets certain mathematical condition. In the following chapter, the fundamental theoretical and algorithmic aspects of CS will be presented.

Chapter 2

Compressive Sensing Theory

The central tenet of the signal processing world is the well-known Shannon sampling theorem which claims that when sampling a signal (e.g., converting from an analog signal to digital) the sampling frequency must be greater than twice the bandwidth of the input signal in order to be able to accurately reconstruct the original image/signal [4]. The major problem of this sampling scheme is that it neglects the fact that almost of the natural images/signals have certain structures embedded. CS goes against the conventional wisdom by asserting that one can recover such signals and images from far fewer measurements than those based on Shannon theory and without detailed knowledge of the signal struction. In essence, CS relies on two principles: *compressibility/sparsity* and *measurement incoherence.*

2.1 Compressibility/Sparsity

Many natural images or signals, when transformed to a proper basis, have sparse representations, i.e. most of their transform coefficients under this basis are equal to or decay very rapidly to zero. Consider, for example, the 1 megapixel image and its wavelet transform shown in Figure 2.1. Although almost all the pixel values of the image in the space domain are non-zero, a majority of its wavelet coefficients are zero or nearly zero. Figure 2.2 displays the reconstructed image with 2.5% of the lead coefficients. We can capture most of its information by keeping only the few largest wavelet coefficients.

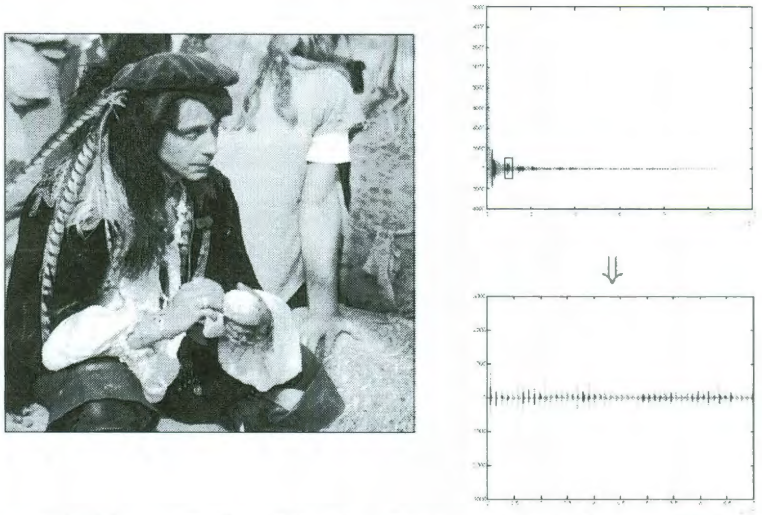

Figure 2.1 A 1 megapixel image (left) and the plot of its wavelet transform coefficients (right)

Figure 2.2 The reconstructed image using 2.5% of the lead coefficients

From the mathematical perspective, let us consider a real-valued signal vector $x \in R^N$ such as the N-pixel image in Figure 2.1. Assuming the signal has sparse representations in an orthonormal basis (such as Fourier, wavelet or Gabor) $\Psi := [\psi_1, \psi_2, ..., \psi_N]$, we can expand x as the linear combination of elements of Ψ as:

$$x = \sum_{n=1}^{N} \alpha(n)\psi(n) = \sum_{m=1}^{k} \alpha(n_m)\psi(n_m) \qquad (2.1)$$

where α and n are corresponding transform coefficients indices. The linear combination is truncated at k because there are only k non-zero significant coefficients and the other $N-k$ coefficients are either equal zero or decay quickly to zero. In matrix notation the equation (1.1) can be expressed as $x = \Psi\alpha$, where x is a length N column vector, the sparse basis Ψ is an $N \times N$ matrix and $\alpha(n)$ is an length N column vector with k non-zero elements. The signal is said to be k -sparse in the Ψ basis in this case. Most of modern compression approaches, such as JPEG, JPEG-2000, exploit the fact that the k significant coefficients contain enough information needed to represent the original signal and the rest of the smaller ones can be discarded without much perceptual loss. CS is also based on this premise, but instead of capturing all the information when acquiring the signal and then transforming and throwing away the small coefficients in the later reconstruction, CS combines acquisition and compression into one step. However, this raises a big question, "How do we know which of the combined measurements will capture the critical largest coefficients?"

2.2 Incoherent Sensing

CS enables us to reconstruct a signal from M << N measurements. But these measurements are not acquired directly in the sparse basis Ψ. Instead they are linear projections of the signal onto a sensing or measurement basis Φ. In matrix notation, the measurements can be expressed as

$$y = \Phi x = \Phi \Psi \alpha = \Theta \alpha \tag{2.2}$$

where y is the $M \times 1$ column vector, measurement basis matrix Φ is $M \times N$, and x (the N pixel image) is the $N \times 1$ column vector.

The coherence [5] between the measurement basis Φ and the sparse basis Ψ is defined as

$$\mu(\Phi, \Psi) = \sqrt{n} \max_{m,n} \left| \langle \varphi_m, \psi_n \rangle \right| \tag{2.3}$$

In plain English, μ measures the largest correlation between two elements Φ and Ψ. The possible range of μ is $[1, \sqrt{n}]$. A smaller μ tends to lead to fewer samples needed in the final reconstruction step. One therefore wants to choose Φ such that μ is as close to the minimum value 1 as possible. In other words, the measurement basis Φ and the sparse basis Ψ should be as incoherent as possible.

To take as an example, the spike basis, which corresponds to the classical sampling scheme in time or space, and the Fourier basis, there are maximally incoherent because they obey $\mu = 1$. Random matrices, in most cases, are incoherent with any sparse basis Ψ, and have broad applications for images whose sparsity might occur in different sparse bases. In our hardware applications, known random projection matrices are implemented

by controlling the flipping directions of the DMD mirrors. A series of measurements are collected by repeatedly changing the patterns displayed on the DMD.

2.3 Sparse Signal Recovery

After the sparse signals are encoded with the small number of linear measurements, an efficient decoder is needed to reconstruct the original data. To recover the length-N signal x, or equivalently its sparse coefficients, is an ill-posed problem because M is much smaller than N and we will have infinite α′ that will satisfy $\Theta\ \alpha\ ' =\ y$. However, with a single piece of additional information, i.e. the signal is sparse in some basis, we can compute the reconstruction uniquely. In this section, I would like to discuss two popular algorithms used in our applications: ℓ1 minimization and total variation (TV) minimization.

2.3.1 ℓ1 Minimization

To recover an image k-sparse α from $y = \Theta\alpha$, we solve an optimization problem. We know that α is the sparsest vector which maps to y, thus it must be the solution to the following optimization problem

$$\min_{\alpha} \#\{k : \alpha(k) \neq 0\}, \text{ subject to } \Theta\alpha = y \tag{2.4}$$

where $\#\{k : \alpha(k) \neq 0\}$ is the number of non-zero terms in the candidate vector α. Solving (2.4) is referred as the ℓ0 minimization problem [6].

However, solving the ℓ0 minimization problem is infeasible and combinatorially expensive [7]. Fortunately, there is a convex program that can work almost as well

$$\min_{\alpha} \|\alpha\|_{l1} \text{ subject to } \Theta\alpha = y \tag{2.5}$$

which is termed as $\ell 1$ minimization. Under favorable conditions [8, 9, 10], minimizing the $\ell 1$ -norm is equivalent to solving the $\ell 0$ minimization problem, which also yields the sparse solutions. Compared with Equation 2.4, the problem in Equation 2.5 is less challenging.

2.3.2 TV Minimization

One important property of the image data is the small differences between the values of adjacent pixels. TV minimization exploits this property to reconstruct the signal from its linear samples [11]. The scheme of TV minimization is to solve the following problems:

$$\min_{x \in R^N} \sum_i \|D_i x\|, \quad \text{subject to} \quad Ax = y \tag{1.5}$$

where $D_i x$ is the discrete gradient of x at pixel i. $\|.\|$ can be either the 1-norm which corresponds to the anisotropic TV, or 2-norm which is isotropic TV in this case.

The TV concept was first introduced by Rudin, Osher and Fatemi [11] in 1992. The detail discussion of the TV mode was reported by Chambolle et al. [12, 13]. In 2004, Chambolle [14] proposed an iterative algorithm for TV denoising and proved the linear convergence. Furthermore, Chambolle's algorithm can be extended to solve image reconstruction problems with TV regularization while the measurement matrix is orthogonal.

Due to the powerful applications of TV model in edge detection, many solvers have been worked out to solve the TV minimization problems. However, most solvers are either too slow or not robust compared with the $\ell 1$ minimization methods. Recently, a new solver named *TVAL3* [15] was developed to overcome these difficulties and we frequently adopt this solver in our image reconstruction process.

Chapter 3

SWIR Imaging System & Its Applications

One may wonder why we need a single-pixel camera when today's megapixel cameras are so cheap. In fact, it happens to be a very fortunately coincidence that the wavelengths where the human eyes are sensitive, also coincide with those that silicon is able to absorb and covert to electrons; and the silicon industry has a long and very mature history on which visible imaging can rely. However, for wavelengths which are invisible to the human retina, they can only be detected by the non-silicon sensors such as InGaAs, HgCdTe or InSb for the infrared regimes. These types of sensors have to mated with traditional silicon readout technology if one want to exploit them as focal plane arrays, which becomes much more expensive. That is why current commercial infrared cameras, compared with visible ones, have lower resolutions and are much more expensive. Our compressive imaging systems have the potential to greatly reduce the costs compared with current infrared imaging technology. The hard to access wavebands of SWIR light and the fact that our visible single-pixel camera system can be easily adapted to imaging in this regime inspired the work introduced in this chapter.

3.1 SWIR light

Human eyes can generally respond to light with wavelength from 400 nm to 700 nm. Wavelengths beyond that range are not detectable. We refer to wavelengths below 400 nm as ultraviolet (UV) and those above 700 nm as infrared (IR). IR can be further broken

down into three primary regions, short-wave infrared (SWIR), mid-infrared (MWIR) and long-infrared (LWIR), with wavelengths from 1.1-3, 3-50 and 50-1000 microns respectively. We will reserve the category of near infrared (NIR) to be the infrared region beyond human vision but still detectable by silicon technology. It should be noted that the invisible light has no "color" per se, since the color is a construct of human perception rather than the absolute property of the light. SWIR light interacts with objects in the same way as the visible light does. What's more, glass lenses transmit SWIR light, while MWIR and LWIR cameras have to use lenses made with more exotic materials, such as fluoride and selenide compounds. Therefore, extending from the visible imaging system to a SWIR setup can be reduced to devising a comparable detector without a complete redesign of the optical system.

3.2 Imaging Applications

Practical applications of the SWIR imaging include the night vision via both heat an atmospheric night glow, food inspection, semiconductor circuit inspection, quality or process control, and art authentication, just to name a few. Below are some examples from our single pixel camera to a few of these endeavors. Note that all the targets in this experiment are illuminated by a halogen lamp with a 900 nm long-pass filter.

3.2.1 Damaged Apple Inspection

Because water is opaque to SWIR light, detecting its presence or absence is very widely used in food inspection technology. For example, bruises under the skin of fruits, an apple in our experiment, are invisible to human eyes or visible cameras, but can be seen from our single-pixel SWIR imager.

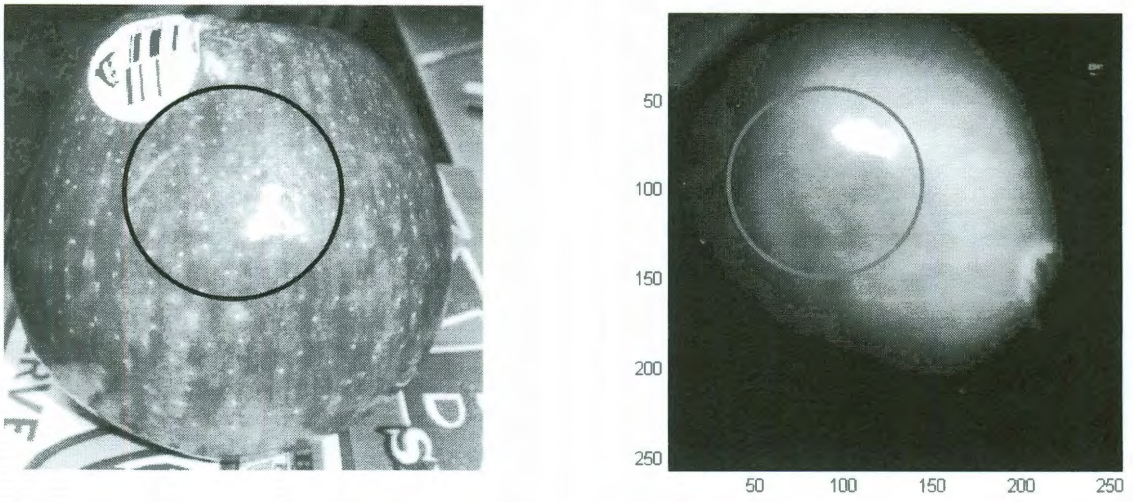

Figure 3.1 Visible view of an apple with the bruise circled in back (left) and the its SWIR image with the same bruise circled in red (right)

3.2.2 Detecting the Fill Level through the plastic

The powder bottle shown in Figure below is opaque to the visible camera. However, our 1-pixel SWIR camera system can see though the same plastics to detect the fill level of the powder inside. Such technology is very beneficial in quality or process control to ensure the product fill level is accurate.

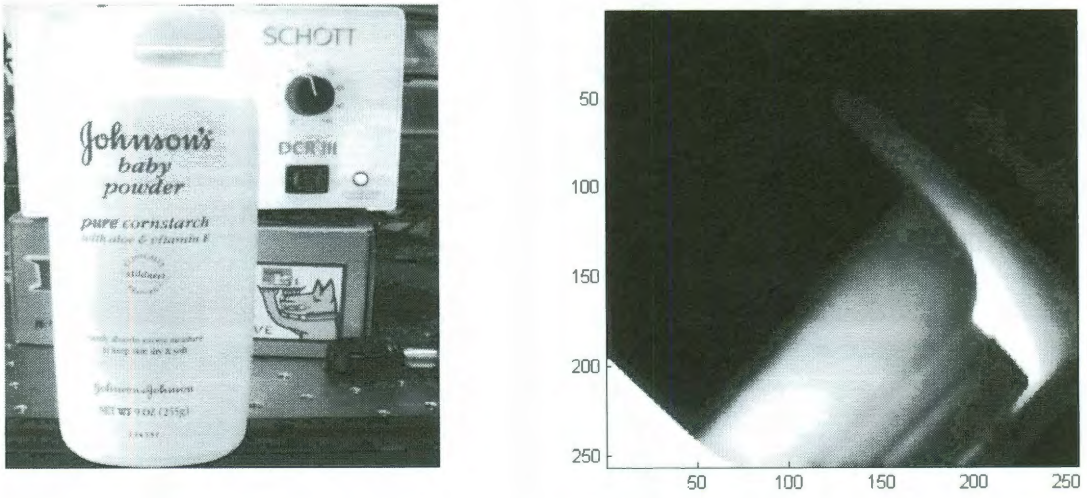

Figure 3.2 Visible view of a plastic bottle filled with baby powder (left) and its SWIR image taken by our SWIR camera (right)

3.2.3 Art Inspection

Many pigments and paints, like aged varnish, are opaque to visible light but very transparent in SWIR portion of the spectrum. Figure 3.3 shows the visible (left) and SWIR (right) views of a test panel painted with a variety of colors of oil-based pigment which are covering charcoal pencil drawings underneath each of the pigment stripes. These color paints are opaque to the visible camera, but pass a significant level of SWIR light, as can be seen by our InGaAs photodiode equipped imager. We further notice that red and yellow pigments are more reflective in the SWIR waveband, compared with the green and blue ones. The black paint absorbs both visible and SWIR light. This response of paint pigments to SWIR light is becoming especially beneficial to the art world for authentication, conservation and preservation of paintings especially since it possesses a nondestructive property that other types of inspection may not.

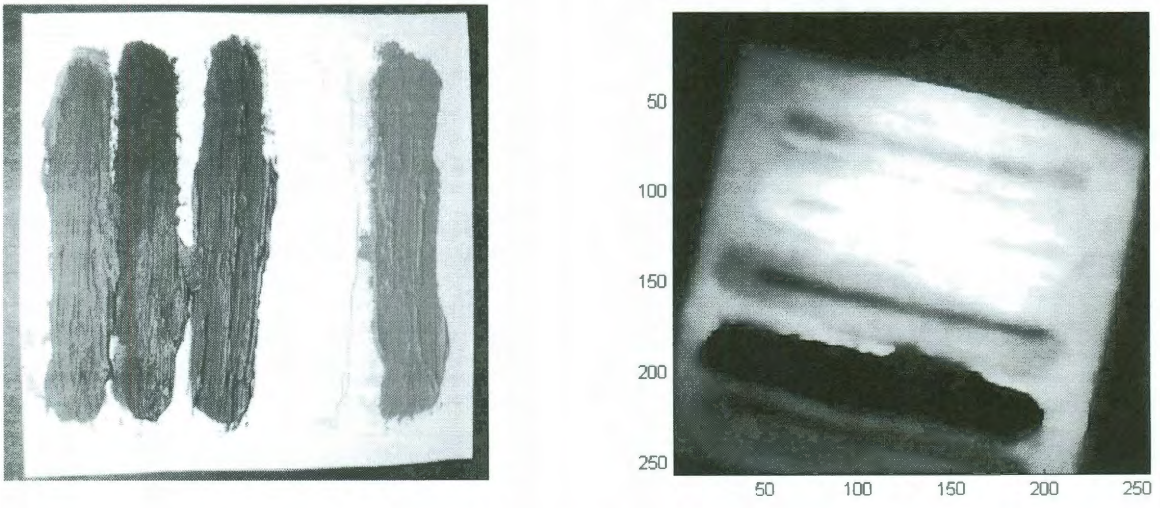

Figure 3.3 Visible (left) and SWIR views (right) of a test panel painted with a variety of colors of oil-based pigment and the charcoal drawings underneath each of the pigment stripes

3.3 Experimental SWIR Architecture

All of the experimental data discussed in this chapter were obtained using the following single-pixel camera system. In this section we introduce our setup in detail.

The design and implementation of our single-pixel camera imaging system successfully validates CS in the imaging applications. Instead of focusing the image of a scene onto a detector array, the image from a biconvex lens is focused onto the DMD functioning as a spatial light modulator. Random projections are multiplexed with the image by controlling the tilt directions of the hundred of thousands of the mirrors inside the DMD, either +12 degree or -12 degree about their diagonals, and the light from the projected image is then all focused down and measured by the single photodetector element. The photodetector measures a voltage for each new projection vector, corresponding to the inner product between each random pattern and the scene. These are then used to reconstruct the original image via nonlinear optimization algorithms. A schematic diagram (top view) of the experimental setup in the lab is shown in Figure 3.4

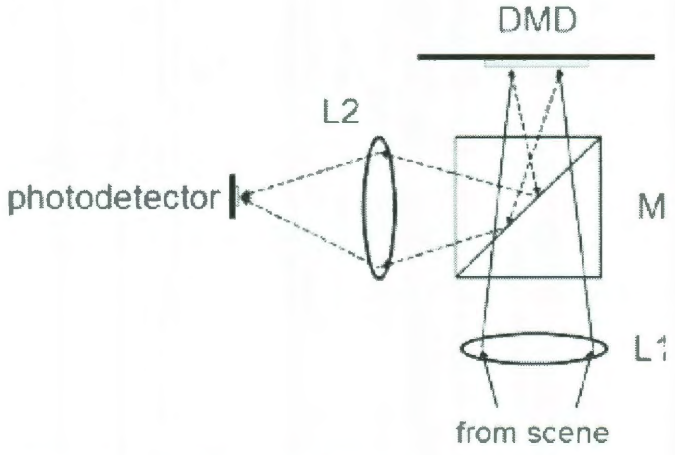

Figure 3.4 The schematic of the single-pixel camera setup

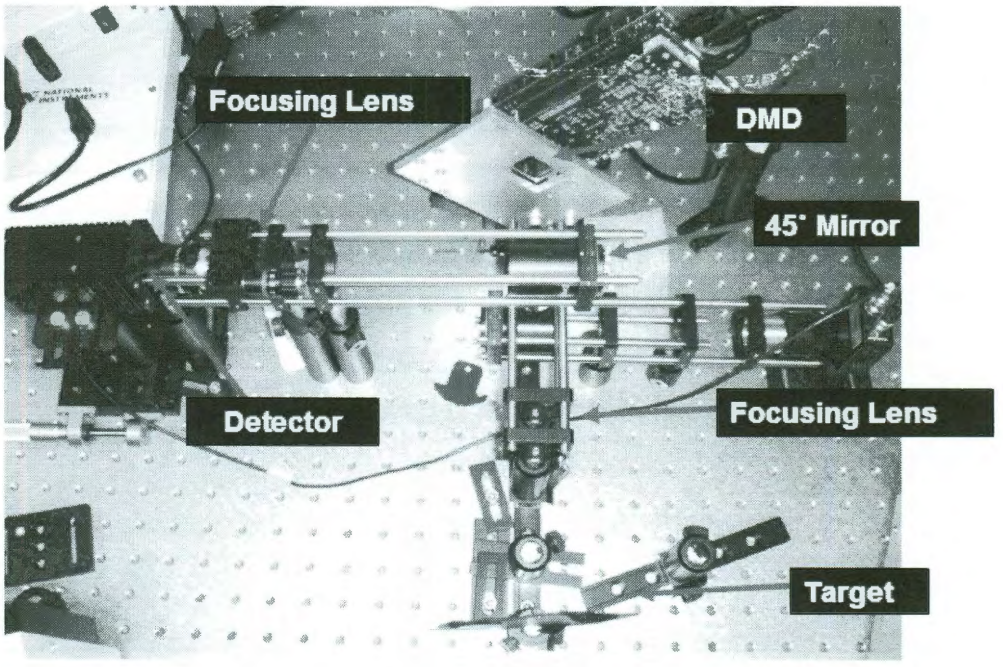

Figure 3.5 The actual lab setup of the single-pixel imaging system

The actual lab setup is displayed in Figure 3.5. The DMD D1100 system, with a maximum resolution of 1024 by 768 and with 96 Gigabits memory on board, is used as the light modulator in this setup. To simplify the alignment of the optical components, the DMD is typically rotated 45 degree to enable the optical plane of incoming light and outgoing modulated light either parallel or perpendicular to the table plane. The 45° mirror is used to direct the outgoing lights from DMD to the detector channel. The detector used in this experiment is an InGaAs IR module (model number G6122 from the Hamamatsu Company). Its spectral response is shown in Figure 3.6. The voltage signal generated by the detector is sent to an 18 bit A/D converter (model USB6281 from National Instrument) which has a dynamic range from -10 V to +10 V.

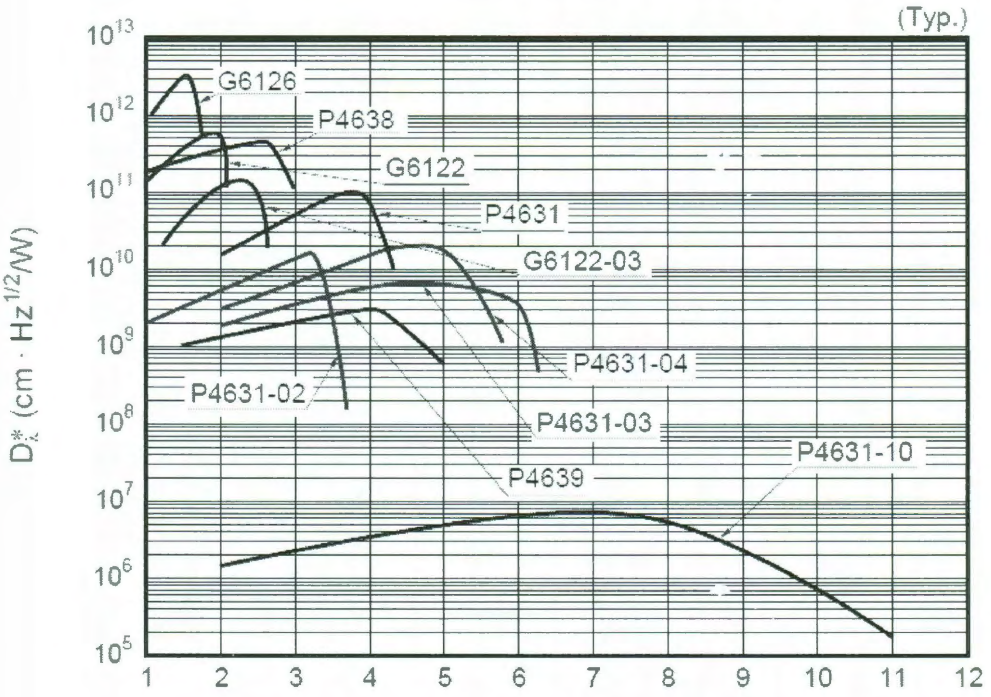

Figure 3.6 Spectral responses of the IR modules from Hamamatsu Company (figure online http://www.hamamatsu.com/)

3.4 Light Modulation

The implementation of random projections is the essential part of the CS based imaging system. Fortunately, the DMD can function as the high-speed light modulator which allows us to display programmable random patterns on it. Liquid crystal devices (LCDs) are also a popular choice for spatial light modulators, but speed, precision, and bandwidth limitations make them less attractive for many applications.

3.4.1 What Is a DMD?

The DMD is an optical micro-electro-mechanical system built from traditional semiconductor technology that is the core of DLP projection technology and was

developed by Dr. Larry Hornbeck and William E. "Ed" Nelson of Texas Instrument in 1987. It allows images to be projected brighter, sharper and more realistically than previous alternative technologies. Figure 3.7 shows the schematic of the DMD in a one-chip DLP projection system.

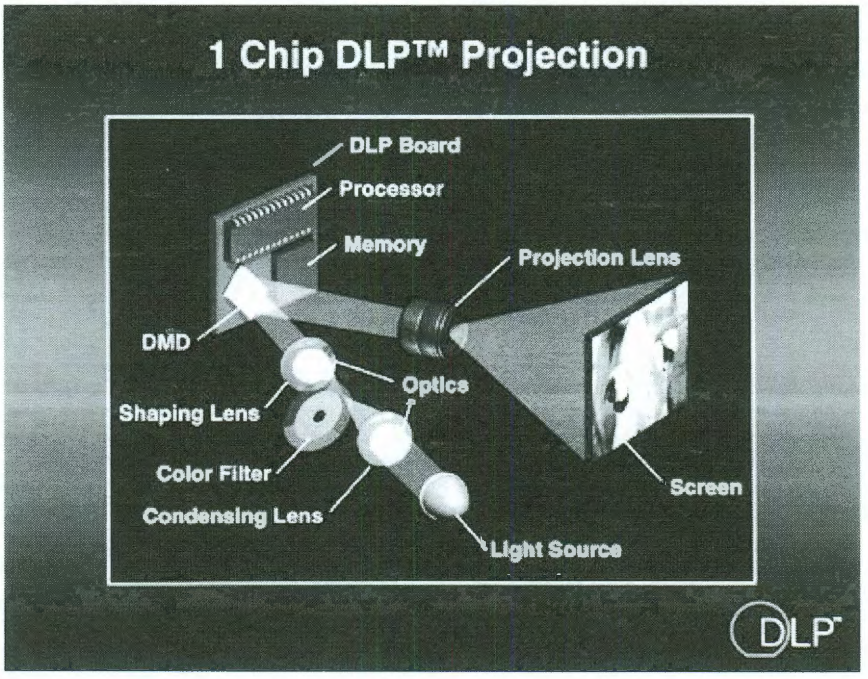

Figure 3.7 The schematic of the DMD in a one-chip DLP projection system
(figure form texas instrument website http://www.dlp.com/technology/how-dlp-works/)

Commercial DMDs are available with varying resolutions. There are two types of DMD chips systems in our lab, the 0.7 XGA and the 0.95 1080p with the resolutions of 1024 × 768 (13 micron mirror widths) and 1920 × 1080 (10 micron mirror widths) respectively. The millions of tiny mirrors employed in the DMD are coated by aluminum, the directions of which can be turned on (towards the lens) and off (away from the lens) thousands of times per second. Typically the DMD is operated at speeds of tens of kilo-

hertz, the maximum achievable speed of one hundred kilo-hertz. Figure 3.8 shows a DMD chip with a zoomed in section showing the microscopic mirrors in comparison to an ant leg.

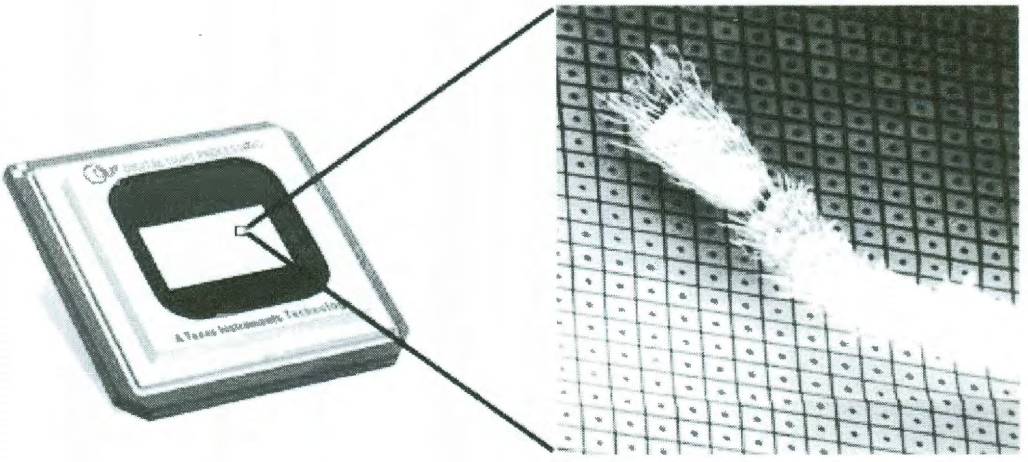

Figure 3.8 DMD chipset with a zoomed section
(http://www.hometheaternetwork.com/HTN_HDTVdlp.htm)

3.4.2 Mechanical Architecture of a DMD Chip

The DMD pixel is an integrated micro-electromechanical system (MEMS) structure that is fabricated over a CMOS SRAM cell. As illustrated in Figure 3.9, the aluminum mirror is rigidly attached to a yoke. The yoke is connected by two thin, mechanically compliant torsion hinges supported by the posts that are connected to bottom substrate. An electrostatic torque can be created by the electrostatic field developed between underlying memory cell, the yoke and the mirror. This force works against the restoring torque of the hinges to rotate the mirror in the positive and negative direction. The electrodes hold the mirrors in place once tilted.

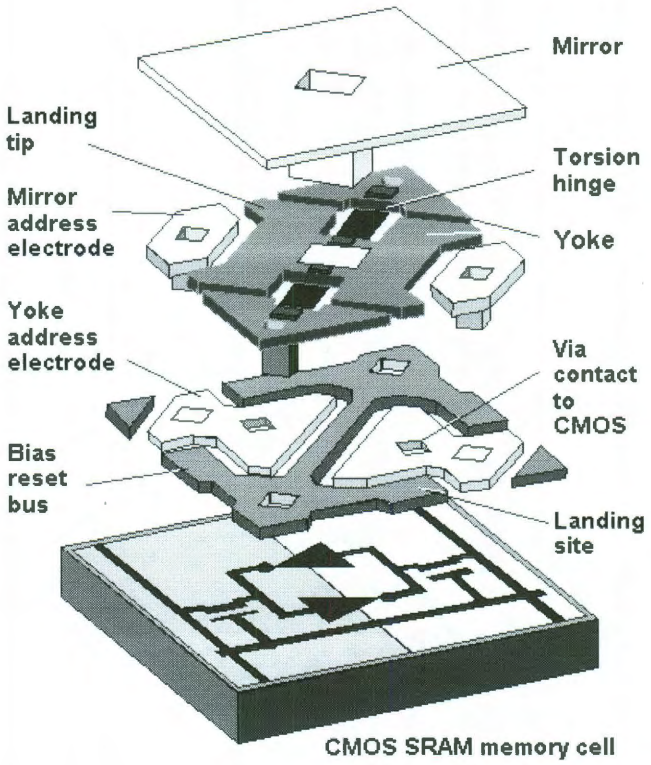

Figure 3.9 Mechanical structure of a DMD chip

(http://focus.ti.com/download/dlpdmd/115_Digital_Light_Processing_MEMS_Timely_Convergence.pdf)

3.4.3 DMD Controller Package: Discovery Board & ALP Board

In the past, DMD applications were mainly focused on the large sales volume devices such as business projections and home cinema. When this technology achieved significant success in these markets, TI began to seek the applications in the non-projector areas. Thus, a variety of DMD components and accessories became available to research and development centers, including university research labs. The DMD Discovery platform was developed for scientists and engineers to prototype new DMD engineering applications. The first release from DLi was the DMD Discovery 1100

development kit, and later Discovery 3000 and 4100 boards were released, each with different mirror array specifications. The Discovery board carries the DMD mirror array and the driver electronics for mirror motion control. Discovery also provides a high-speed parallel data interface to the accessory light modulator package (ALP) board.

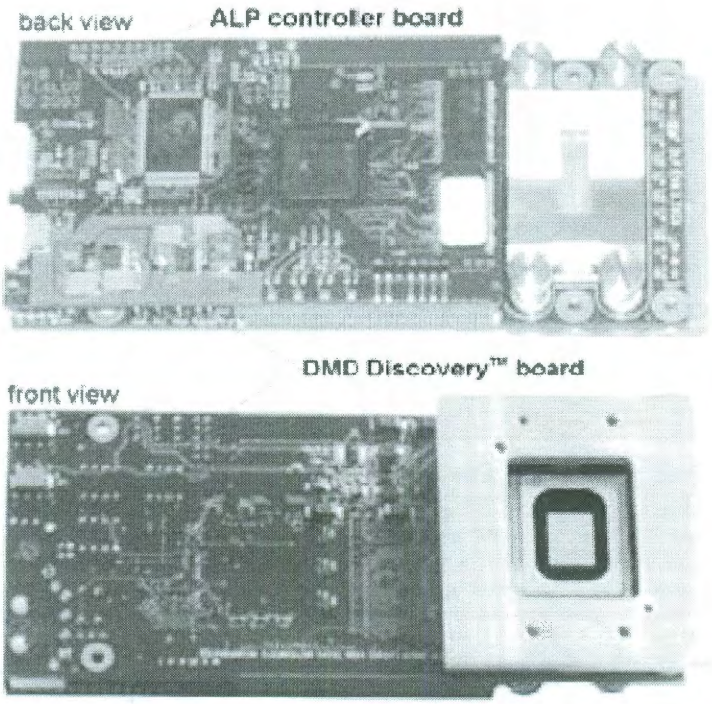

Figure 3.10 DMD Discovery board and ALP controller board for D1100

Based on the Discovery platform, Vialux, GmbH developed the ALP parallel interface controller for high speed DMD operations that require the loading of large image sets to the mirror array. Used with the Discovery Controller Board, the ALP is a turnkey tool that provides simple, direct, and fast access to any single mirror. The main ALP components are sketched in Figure 3.11:

- USB controller with PC

- SDRAM for frame storage
- FPGA for high-speed data control

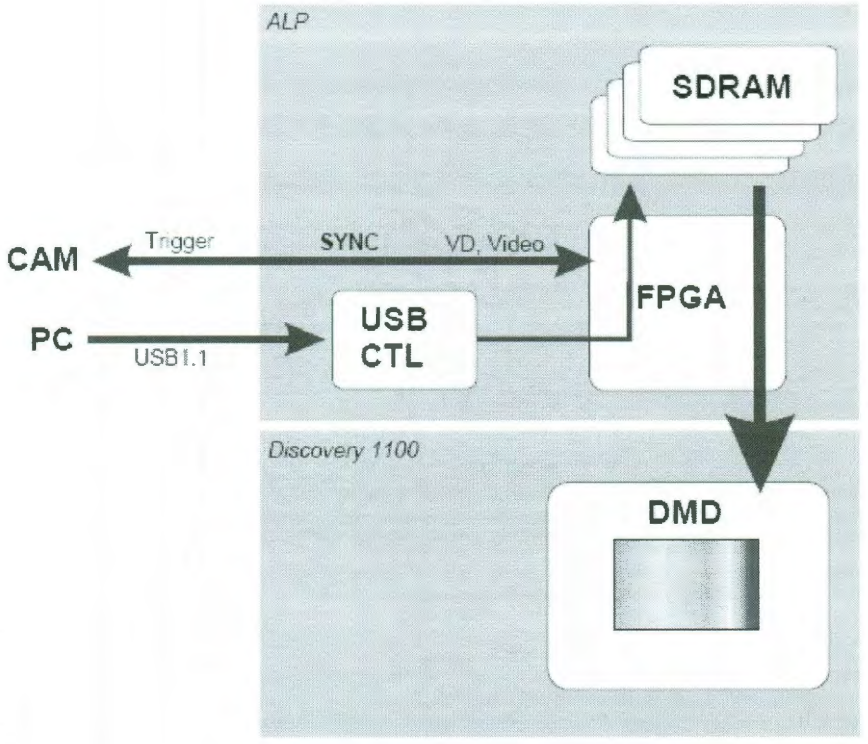

Figure 3.11 Sketch of the main ALP components (Proc SPIE, Vol. 5289B, Electronic Imaging, San Jose, 2004)

Accordingly, the development of ALP interface board enables us to preload and store the pattern sequences on the DMD controller board, which are then transferred to the micromirror array and displayed at the maximum DMD frame rate.

3.4.4 Spectral Responses of the DMD Windows

The sealed glass window of DMD is coated with an anti-reflection layer. Coating materials can vary according to different applications in different wavelength ranges. Figure 3.12 shows the transmission spectra of various UV, VIS and near-infrared (NIR) windows made by TI and based on BK-7 materials compatible with the technology needed to seal the DMD chip.

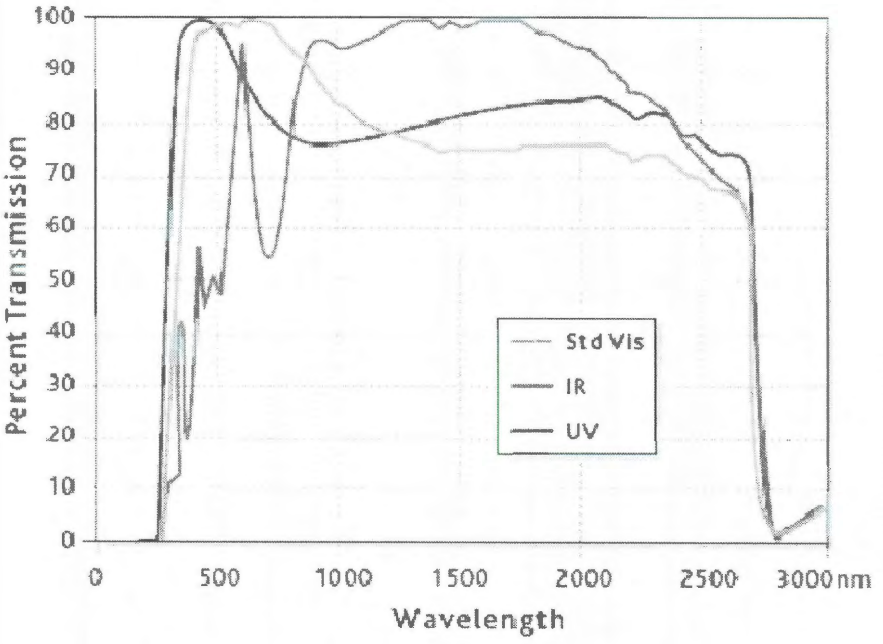

Figure 3.12 The transmission spectra of UV, VIS and NIR windows from TI

To explore the imaging and spectroscopic applications in mid-infrared (MWIR) and long-infrared (LWIR), we bought DMD chips retrofitted with ZnSe and BaF2 windows from Optical Science Corporation (www.opticalsciences.com). Their transmission spectra are shown in the top and bottom of Figure 3.13, respectively.

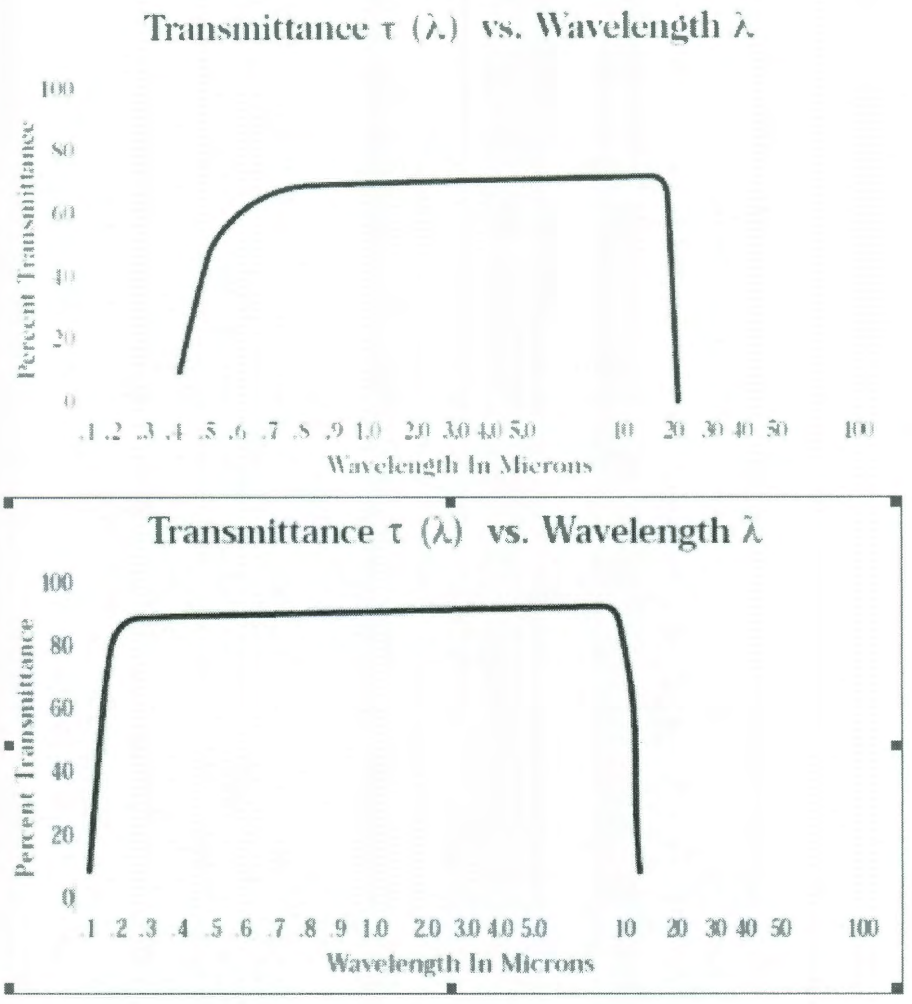

Figure 3.13 Tansmission spectra of ZnSe (top) and BaF2 (bottom) windows from Optical Science Corporation

3.4.5 Pseudo-Random Measurements

Random matrices are the ideal measurement basis for CS because they are incoherent with all known sparse basis. Meanwhile, these patterns are not desirable because it is extremely computationally expensive in the final image reconstruction process due to the lack of an efficient inverse transform. Fortunately, there exist the fast Walsh-Hadamard

inverse algorithms [16, 17] that can yield very faster image reconstructions. Thus, in our experiments, a permutated Walsh-Hadamard matrices which elements are half zeroes and half ones are transmitted and displayed on DMD. To ensure randomness, first, the elements of each Walsh-Hadamard frame (measurement vector) are permuted by bit reversal ordering and then the order of frames are also permuted. The examples of four 32×32 random patterns used are displayed in the Figure 3.14 below. One can see that after such permutations, these matrices possess the properties desired in a measurement basis amenable to the CS mathematics.

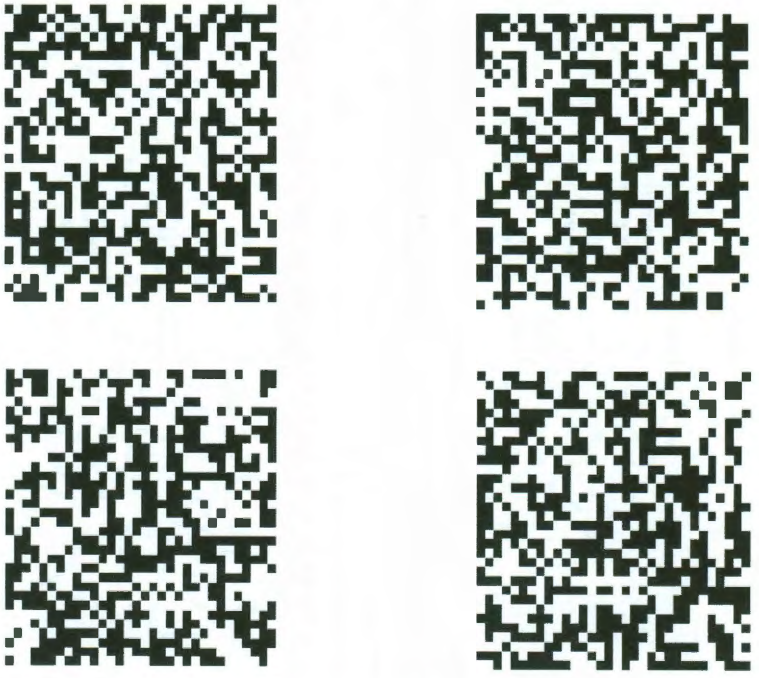

Figure 3.14 Examples of 4 32×32 random patterns displayed on DMD

3.5 High Resolution SWIR Images

The *TVAL3* solver based on TV minimization is used to reconstruct the images shown in this section. The light source in this experiment, shown in Figure 3.15, is a self-made 4 ×

4 LED (1450nm wavelength) array sealed in a box. The box has an open window with a diffuser covering it. The test targets mentioned below are printed on overhead transparencies and back-illuminated by the LED box.

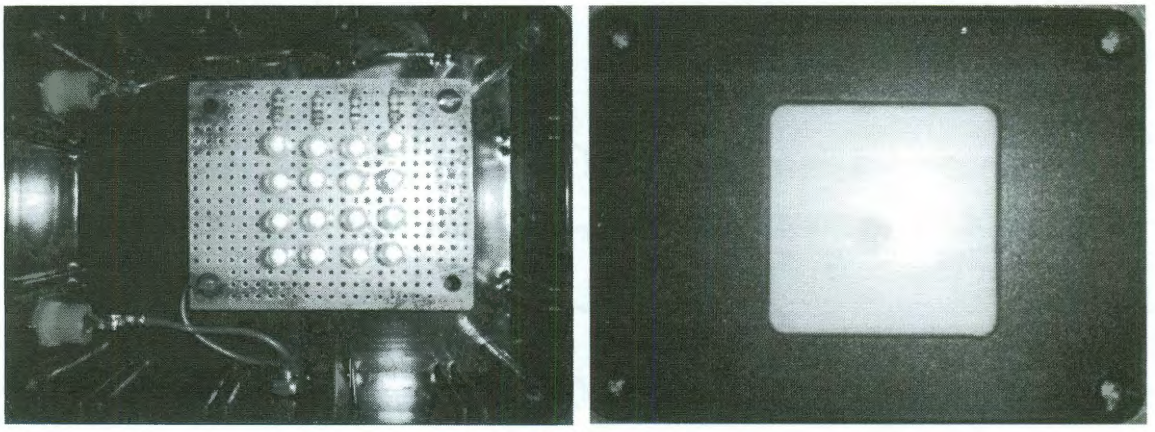

Figure 3.15 The light source box with the 4 × 4 LED arrays inside (left) and a window with the diffuser on it (right)

The first test target is a 512×512 gray scale "Lena" image, shown in Figure 3.16, printed on a transparency. The CS reconstructed images (colormap hot) at the resolution of 256×256 with the 20% percent measurements and 512×512 with the 10% measurements are displayed in Figure 3.17.

Figure 3.16 A 512×512 gray scale "Lena" image

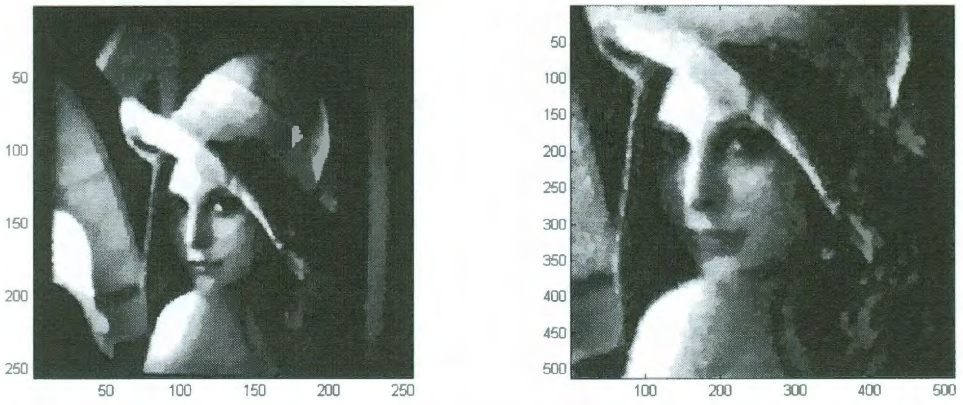

Figure 3.17 Reconstructed images at the resolutions of 256×256 with the 20% percent of the total measurements (left) and of 512×512 with the 10% measurements (right)

Another target used is a custom image made from the varying resolution pieces from the common air force target, shown in Figure 3.18, with the full resolution of 618 × 800. We pieced the different parts together using Adobe Photoshop and printed them on the transparent film. The red boxes in Figure 3.18 indicate the resolution parts used for the target. Figure 3.19 displays the reconstructed images.

One may notice that the reconstructed images at the resolution of 512 x 512 seems larger, compared with those of 256 x 256. This is attributed to the smaller DMD area used at this resolution. For resolution of 256 x 256, 768 x 768 DMD mirror area is used, which means three mirrors operate as a block; for resolution 512 x 512, only 512 x 512 square area on the DMD is active, so in this case each mirror is working independently. But now we can utilize the whole DMD area with 1024 x 768 pixels for D1100 system by padding the measurement matrix to the size of 1024 x 1024 when doing the reconstruction. As a result, we can have a larger working DMD area which also means more light intensity at the detector side. What's more important, the use of the whole DMD area will be a big advantage of our CS system imaging in the IR range when there is a need for very high resolution image. So far no commercial IR camera can achieve the resolution of 1024 x 768.

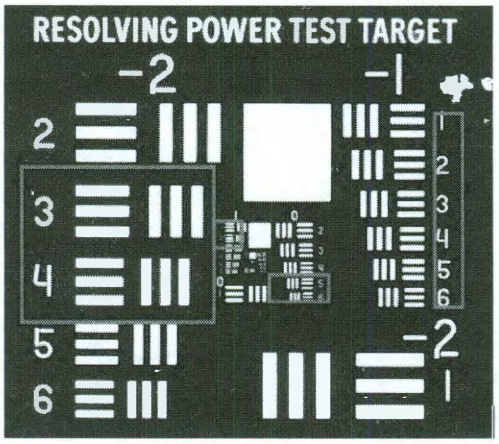

Figure 3.18 A 618 × 800 air force target with the selected resolution regions used in our artificially constructed target marked in rea

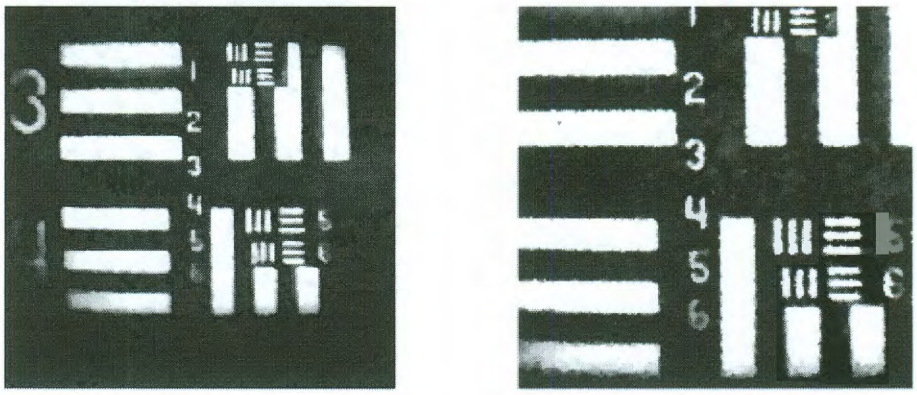

Figure 3.19 CS reconstructed images at the resolutions of 256×256 with 20% coeffs (left) and of 512×512 with 10% coeffs (right)

3.6 Conclusion

CS is a very powerful theory which reveals that a small group of non-adaptive linear projections of a compressible signal or image contains sufficient information for a high quality reconstruction. The design of the single pixel camera exploits this idea in the case of imaging by directly acquiring random projections of a scene without first collecting measurements equal to the total pixels in the image. One of the great benefits of this architecture is its ability to get an image, or even a video, with a single detection element while sampling the scene many fewer times than the number of pixels. For some wavelengths outside the visible spectrum, where it may be too expensive to produce the large detector arrays, this scheme yields similar solution while using only one detector element. As will be discussed in the next chapter, this design can be modified to create a single pixel spectrometer by insertion of one or more diffractive elements, which will exploits the same ideas presented here, to obtain the desired spectrum with a single detective element as opposed to the detector array presented in most systems. In addition, the acquisition of far fewer than ten or twenty percent of measurements will be shown to still be beneficial for reconstructing the spectral signatures.

Chapter 4

Compressive Echelle Spectrometer

Capturing the input of dispersed light, generating a hyper-colorful "rainbow" in the visible case, our single-pixel camera system can function as a high resolution spectrometer. High resolution and wide band coverage are achieved simultaniously by combining an Echelle grating and a second cross-disperser, such as a low dispersion grating in our setup. While this chapter will demonstrate the initial feasibility of such a system in the visible part of the spectrum, our CS method is especially beneficial when you move into the infrared where two-dimensional focal plane array costs skyrocket from $50 for a 5 megapixel silicon sensor to $500,000+ for a quarter of megapixel because of the necessity of InGaAs to detect infrared light. One of the important applications of our single pixel Echelle spectrometer will be as a gas sensor for chemical detection and identification. By combining this with the idea of the compressive matched filter, we can detect and classify the components of the gas composite by using far fewer compressive measurements than would be necessary for computing the full image reconstruction.

In this chapter, we first introduce the principles of Echelle spectrometers; then we discuss our visible single-pixel Echelle spectrometer testbed including the optical setup and experimental results to demonstrate the feasibility of the design. Finally, plans for future infrared applications with modeling will be provided.

4.1 An Echelle Grating Fundamentals

The basic information needed to understand the general features of the Echelle spectrograph will be provided in this part. For more thorough discussions, the interested reader is referred to more comprehensive review papers [18, 19, 20, 21].

The term *Echelle* denotes a special diffraction grating with rather coarse groove spacing (23-316 grooves/mm available from Newport Company) used at high angle of incidence (typically 32°, 44°, 63.5°, 71.5°, and 79°) which possess high diffraction orders (usually 10-100). Some important properties of Echelle gratings are listed below.

4.1.1 Cross Dispersion

Gratings are used to produce a double series of the repeated spectra through diffraction. Figure 4.1 shows the typical diffraction pattern of the grating. The spectra closest the center are the 1st orders. The traditional spectrographs, which generally use one dispersive element, either a grating or prism, usually operate in 1st or 2nd order.

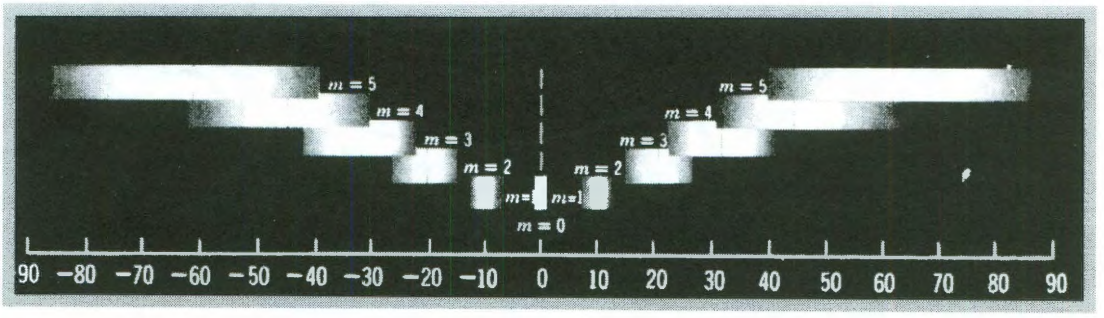

Figure 4.1 Typical diffraction patterns of a grating

However, any Echelle grating is specially designed to work in very high diffraction orders resulting in the overlapping between successive orders. Thus, a second dispersive

element, either a prism or low dispersion grating is needed to disperse the light in the direction perpendicular to the Echelle grating in order to separate these overlapping orders. The resulting two-dimensional spectrum (called an Echellogram), which is a stack of the spectra from successive orders, can be ideally projected on a two-dimensional detector such as a CCD or CMOS camera. A sample Echllelogram taken by a CCD camera from our system is displayed in Figure 4.2. The spectrum goes from deep blue at the bottom left corner to far red at the top right corner. The five spots in the picture correspond to different wavelengths from the argon spectral calibration lamp, which clearly show that each line is a continuous progression of spectral information and not just a single wavelength spread in a second dimension.

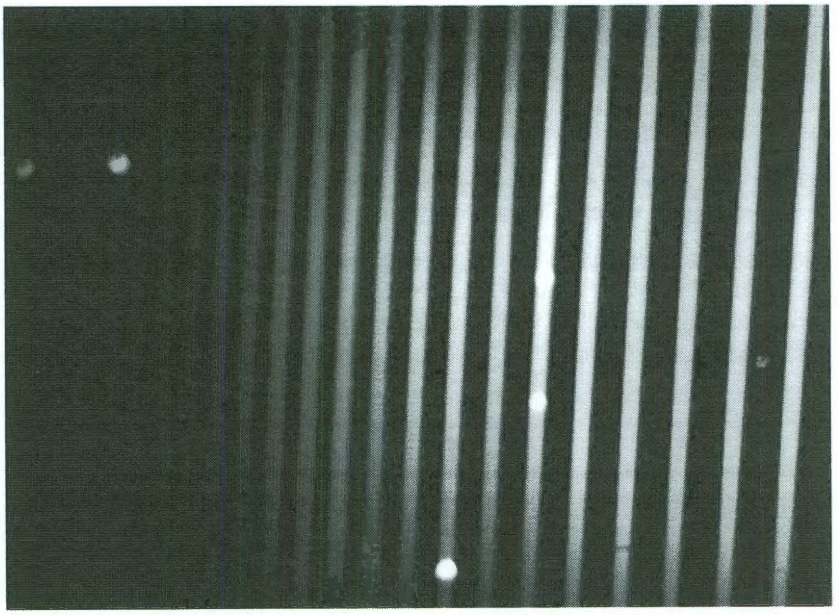

Figure 4.2 A sample Echllelogram taken by a CCD camera from our system

4.1.2 Angular Dispersion

Two perspectives of the Echelle grating (from Schroeder, D. J. 1970. Publ. Sstron. Soc. Pac. 82: 1253-1275) are shown in the schematic in Figure 4.3, where α, β, and θ_B are the incidence, refraction and blaze angles in the YZ plane, and γ is the angle between the incident light and the YZ plane, and σ is the groove spacing of the Echelle. When the light strikes the Echelle at an angle θ, the diffraction equation is

$$m\lambda / \sigma = \cos\gamma(\sin\alpha + \sin\beta) \tag{4.1}$$

where m is the order number for wavelength λ. Thus, for constant α and γ, the angular dispersion is

$$d\beta / d\lambda = m / \sigma \cos\gamma \cos\beta = (\sin\alpha + \sin\beta) / \lambda \cos\beta . \tag{4.2}$$

When the Echelle is in the Littrow arrangement $\alpha = \beta = \theta_B$, for a give wavelength, the angular dispersion becomes

$$d\beta / d\lambda = (2 / \lambda) \tan\theta_B \tag{4.3}$$

For a normal first order grating, typically $\tan\theta_B$=1/2, while for an Echelle grating with the blaze angle of 63.5°, $\tan\theta_B$= 2. Thus, an Echelle gives a much higher angular dispersion than a low blaze-angle grating.

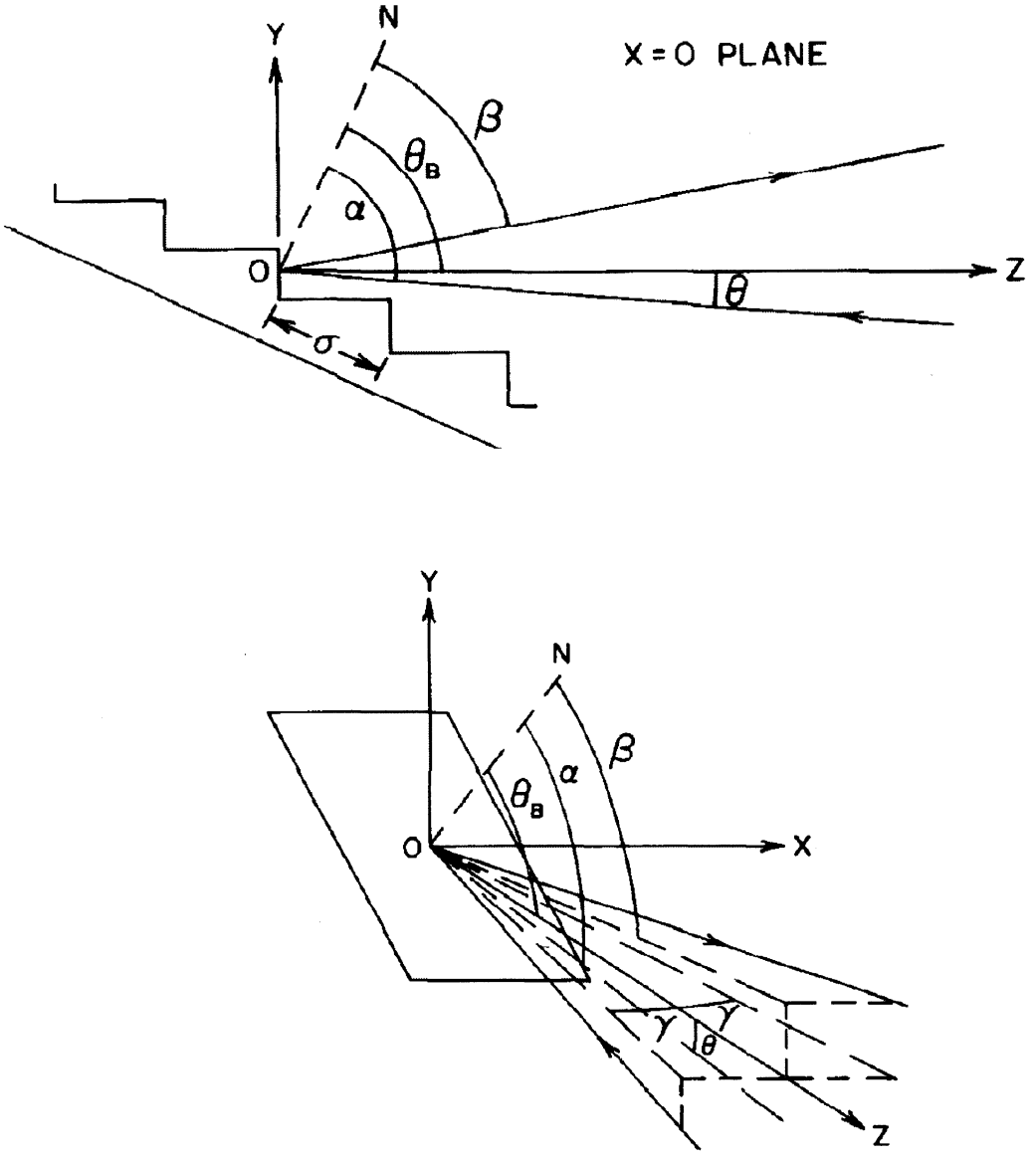

Figure 4.3 Two views of the Echelle section (from Schroeder, D. J. 1970. Publ. Sstron. Soc. Pac. 82: 1253-1275)

4.1.3 Resolving Power

The resolving power R of a grating is a measure of its ability to separate adjacent spectral lines of average wavelength λ. Normally, it is expressed as the dimensionless quantity

$$R = \lambda / \Delta\lambda = mN \tag{4.4}$$

where N is the total number of grooves in the grating. If let W denote the ruled width of the grating, $\sigma = W / N$, and Equation 4.1 becomes

$$m\lambda = \frac{W}{N}\cos\gamma(\sin\alpha + \sin\beta) \tag{4.5}$$

When the Echelle is used in Littrow mode, combining Equations 4.4 and 4.5, we get

$$R = (2W\sin\theta_B)/\lambda = 2D\tan\theta_B/\lambda \tag{4.6}$$

where D is the beam diameter prior to entering the Echelle grating. Therefore, for a give collimated beam size, an Echelle grating delivers a higher resolving power.

4.1.4 Free Spectral Range

If a grating is operating in the Echelle mode, for a give angle of incidence, there are many wavelengths corresponding to different values of m that will be diffracted in the same direction. The relationship between the wavelength and the orders is

$$m\lambda = \sigma(\sin\alpha + \sin\beta) = (m+1)\lambda' \tag{4.7}$$

The difference between these two wavelengths is

$$\Delta\lambda = \lambda - \lambda' = \lambda'/m \tag{4.8}$$

$\Delta\lambda$ is called the free spectral range and is the wavelength interval covered by one order in the Echelle without aliasing.

Figure 4.4 (cited from the lecture of Astronomy A525 class of Dr. Terry Herter, Cornell University) shows the plot of the grating equation solutions for various orders of a grating operating in the Littrow mode. We can clearly see that the same wavelength can appear in different orders, especially when λ is small or m is big.

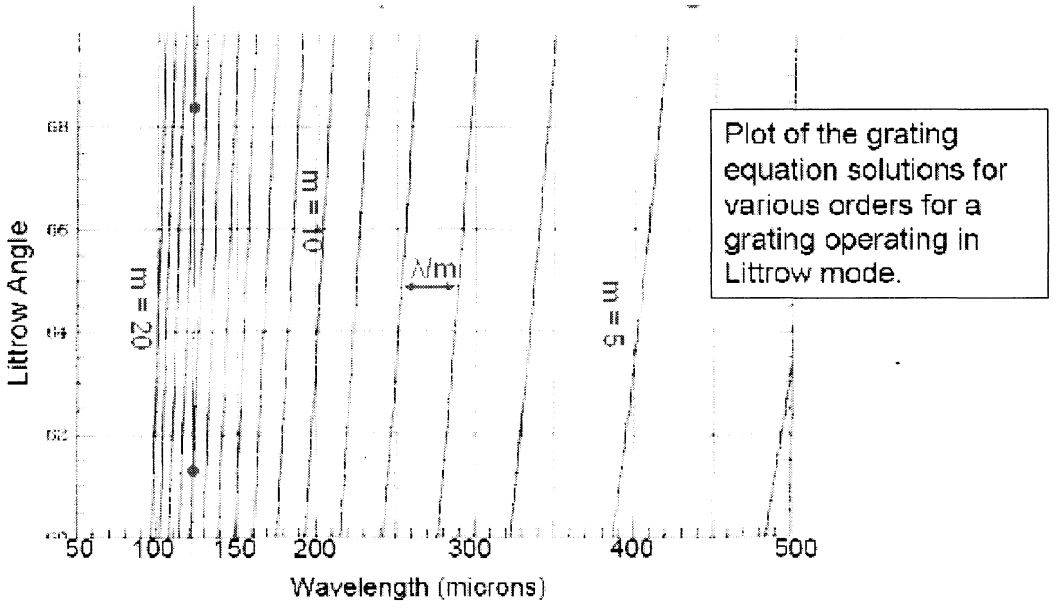

Figure 4.4 The plot of the grating equation solutions for various orders for a grating operation in the Littrow mode (http://astrosun2.astro.cornell.edu/academics/courses/a525/lectures/A525_20%28Echelles%29.pdf)

4.2 Experiment Setup

4.2.1 The Standard Configuration

Figure 4.5 shows a sketch of the conventional Echelle spectrometer setup adapted from the technical note of the Newport Company. The light from a slit or pinhole is collimated, usually by a concave mirror as shown, and then strikes the Echelle grating. The Echelle grating is tilted at the blaze angle for the Littrow mode and another cross disperser, a prism in the picture, is used to separate the overlapping orders after it scatters from the Echelle grating. The resulting two-dimensional spectrum is focused by a camera mirror onto a focal plane array detector.

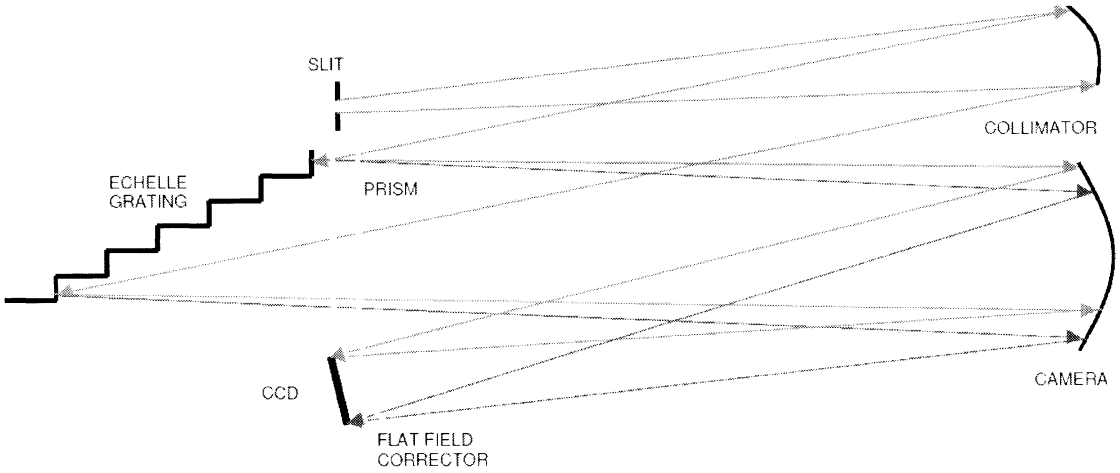

Figure 4.5 Sketch of a conventional Echelle spectrometer setup (technical note of the Newport Company)

4.2.2 The Single-pixel Echelle Spectrometer Setup

Figure 4.6 is a Zemax schematic of our compressive Echelle system.

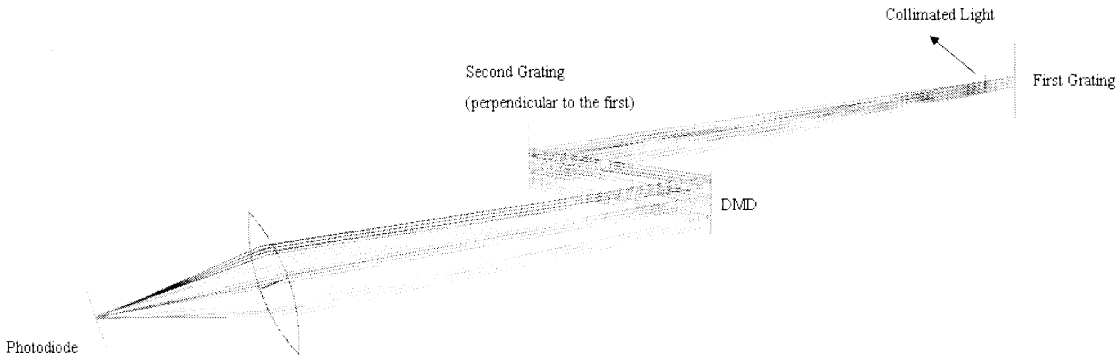

Figure 4.6 Sketch of our compressive Echelle spectrometer setup

In this case, the CCD camera is replaced with the light modulator DMD on which series of random patterns are projected. Light reflected from the DMD is focused by a

lens onto the single detector. Table 4.1 lists the specification of all the elements used in our visible setup.

Light Source	Schott DCR III fiber optic illuminator 150 Watt halogen lamp
Pinhole	300μm aperture diameter
Collimator	Ø2" silver-coated concave mirror, f=150 mm
Echelle Grating	25mm x 50mm, 54.5 grooves/mm, 46° blaze angle, working in Littrow mode
Cross Disperser	Visible transmission grating, 300 grooves/mm, 17.5° blaze angle, 25 x 25 mm
First Focusing Element	Ø2" achromatic doublet, f=100 mm, ARC: 400-700nm
DMD	D1100 with 96 Gigabits memory on board
Second Focusing Element	27.5mm EFL focusing instrument eyepiece
Detector	A photomultiplier (PMT) module, model number H9306-03, from Hamamatsu Company, wavelength range185-900nm, peak wavelength 450nm, rise time 1.4ns, effective area 13mm

4.3 Experimental Results

A series of photovoltage values, which, to reiterate, are the inner products between the two-dimensional Echellogram and random patterns, are collected by the PMT. The *TVAL3* solver is used as the reconstruction tool for results shown in Figure 4.7.

As is evident from Figure 4.7, the ratio of measurements to resolution required for the reconstruction of the same or even better quality of image drops with the increase of the resolution. This phenomenon could be attributed to the fact that the sparsity of the image does not increase as fast as the resolution increases, and thus relatively fewer percent of measurements are needed in the reconstruction step. To better show how the wavelengths spread along different lines/orders, several cutoff filters are inserted just after the light source. The resulting spectra at a resolution of 256 x 256 and 20%

measurements are shown in Figure 4.8. These data can also be used for future wavelength calibration analysis. As is displayed in Figure 4.8, all the visible wavelength range (400 ~ 700nm) should be covered. It is also evident that the same wavelength does appear in different orders, which will give higher intensity when we add together overlapping orders.

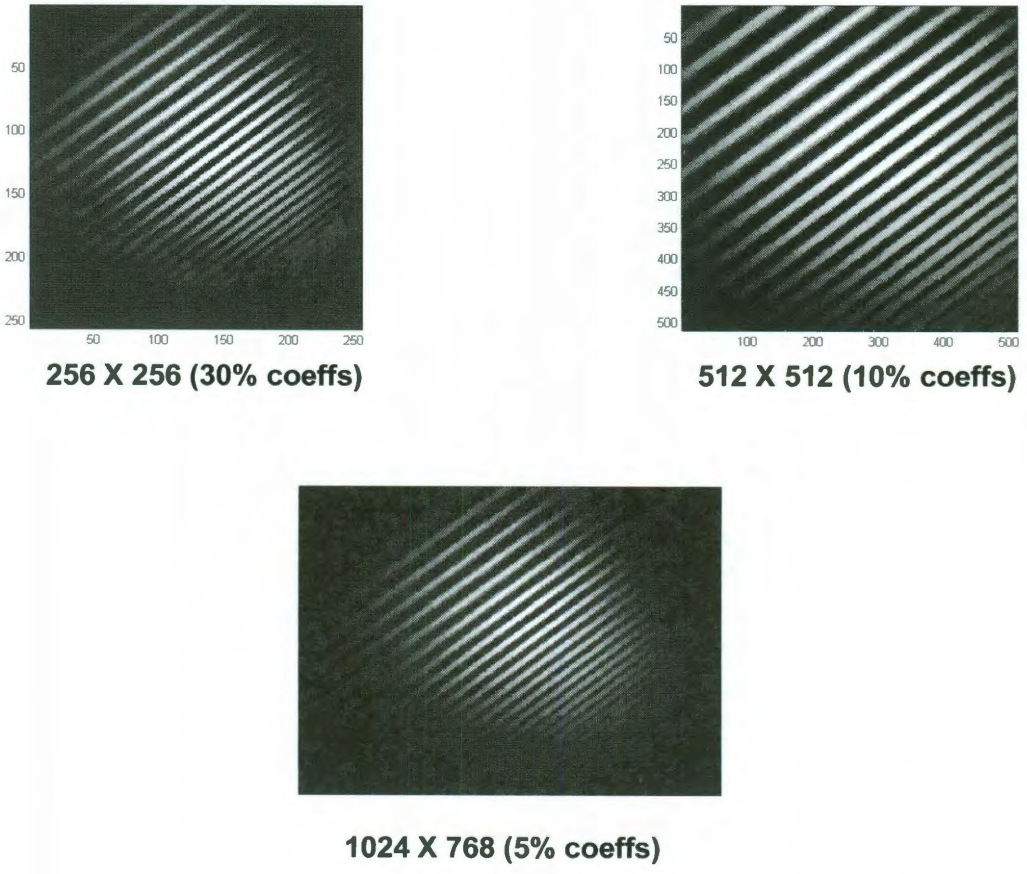

Figure 4.7 Reconstructed Echellogram at different resolutions

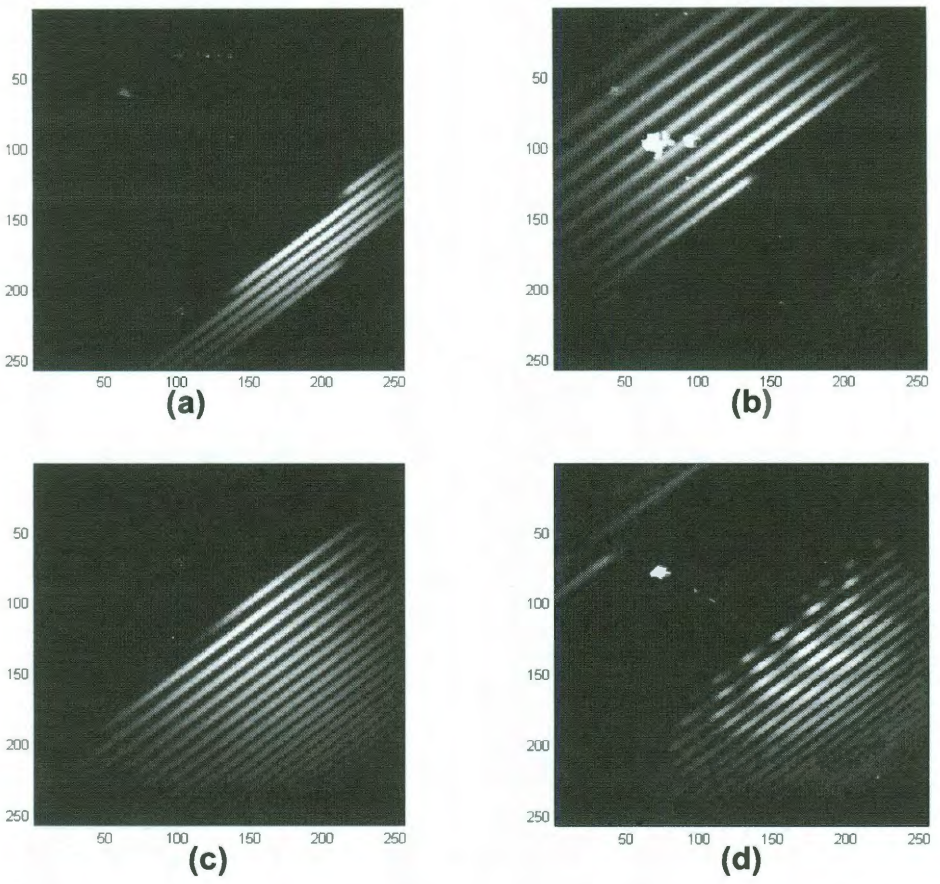

Figure 4.8 Reconstructed spectra with (a) 500 – 550nm band pass filter (b) 633nm long pass filter (c) 650 short pass filter (d) 785nm Raman long pass filter

4.4 Modeling CS Infrared Applications

Having demonstrated a proof-of-concept of CS spectrometer prototype operating in the visible, the following discussion will relate how this could be applied in the IR spectral band. As mentioned above, compared with its counterpart, our system will greatly reduce the cost when doing the spectroscopic applications beyond visible. Figure 4.9 shows the absorption spectra of several types of gases. A quick inspection reveals that many of

them are overlapping. If we hope to create an efficient IR gas sensor with our compressive system, we will need to combine this with an effective mathematical method that addresses this complicated multiplexing. What follows is our modeling of how we will implement such a system to detect target gases with far fewer measurements as compared to the case of imaging.

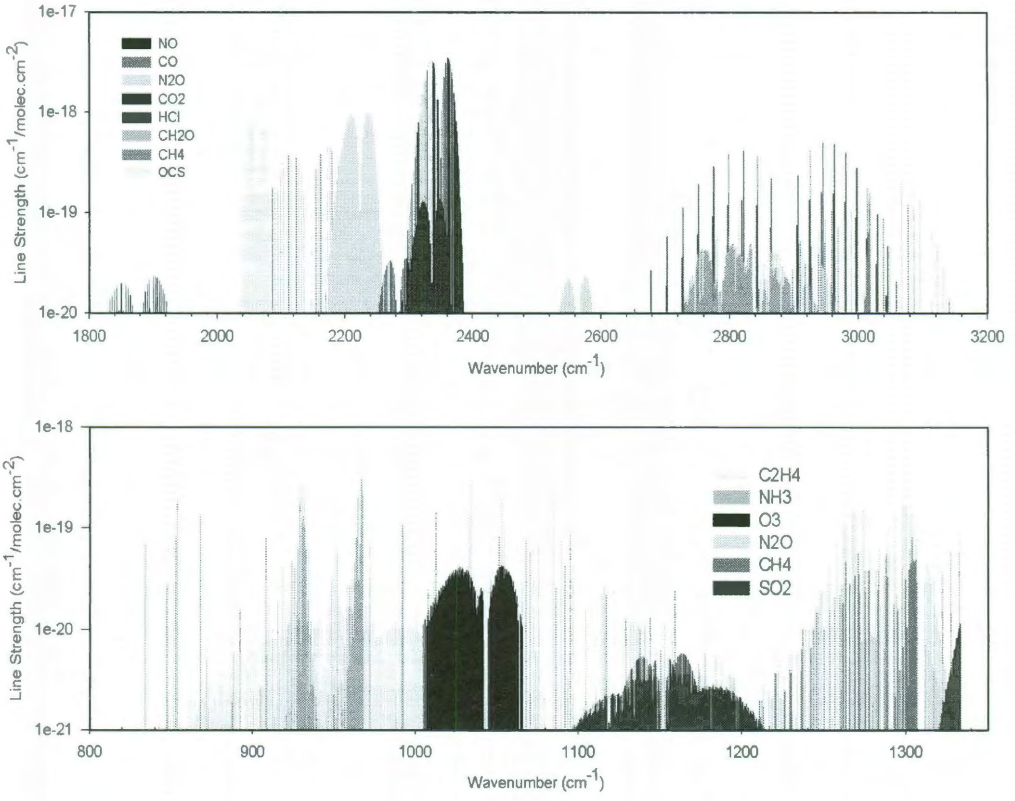

Figure 4.9 Sample absorption spectra of several types of gas from HITRAN database, courtesy of Prof. Frank Tittel at Rice University

4.4.1 Smashed Filter for Spectral Target Classification

CS enables us to recover an image from a set of random projections by exploiting its sparsity in some basis. However, in some applications, we are not interested in reconstructing a complete, precise image of an object, but rather want to detect the presence, orientation or perturbation assuming we know some properties of the object.

Davenport, et al, combined the generalized maximum likelihood hypothesis (matched filter) with compressed sensing and worked out a new technique dubbed the "smashed filter" for classification of objects in the spatial domain [22]. The smashed filter concept is that, for classification and detection purposes, we can directly analyze the compressive measurements, which are very small in number when compared to the reconstruction of the overall image. This work expands on this idea for classification in the infrared spectral domains.

4.4.2 Matlab Simulation Results

We performed a simulation in Matlab to test the effectiveness of the smashed filter for gas classification in IR. This work was done in preparation for and to be couple with DMD chips with ZnSe and BaF2 windows from Optics Science Company. The maximum cutoff wavelength of the IR window on a DMD chip could reach is approximately 2.8 microns, which is clearly shown in Figure 3.8. Fourteen different gases with the absorption spectra in the range of 1 ~ 2.8 microns (corresponding to the wave number from 3571.4 ~ 10000 cm^{-1}) were chosen as the simulation test targets classification in the SWIR. The gases included are C_2H_2, CH_4, CO, CO_2, H_2O, HBr, HCl, HF, HI, N_2O, NO, O_2, O_3, and OH and are numbered from 1 to 14 respectively. Their absorption spectra over this waveband can be seen in Figure 4.10.

First, we chose 4 gases C_2H_2, CO, CO_2 and O_3 to generate a composite test gas with the percentage of 15, 20, 60 and 5 respectively. As an aside, our system is not designed to compete with the trace gas detection system looking for parts per million as in the case for quantum cascade based laser apparatus. Instead, with the production of the DMD chip set in tens of dollars depending on the resolution, we envision a low cost yet effective gas

sensing detector system. Their individual spectra and the total spectrum are shown in Figure 4.11. We use the *SPGL1* solver [23, 24] to perform the L1 optimization. The followings illustrate some of our preliminary results from such a simulation.

In the noiseless case, as revealed in Figure 4.12, for a spectrometer system with the resolution of 6500 pixels, which is close to our current prototype system, as few as 30 percent of measurements (about 0.46%) can yield a perfect detection with the mean square error equal to 0.006. In places where one observes only the red circle, the red (recovered coefficients) are overlapping with the blue (original coefficients). However, in the real world, we can not avoid noise, so we add noise (the magnitude is about 10 percent of that of the original signal) in the test spectrum which is shown in Figure 4.13 with certain spectral part enlarged. In this case, for a spectrometer system with 256 pixels which is the typical resolution for a commercial IR spectrometer, even with 100% measurements, it fails to distinguish between the 4 gases apart. When we increased the resolution back to 6500, the same number of 256 measurements (3.93%) can roughly detect all 4 gases. Increasing the total measurements by less than a factor of two up to 400, which corresponds to 6.15% of the total resolution, we can precisely tell them apart. The corresponding results are displayed in Figure 4.14, 4.15, and 4.16 respectively. The simulation shows the effectiveness of the smashed filter method for spectral target detection in the compressive sensing field. We also notice here that the success of this method also depends on the optical resolution of the system. This motivates the development of a compressive Echelle system which can give higher resolution while preserving the overall low cost. Our future work is to physically combine the smashed

filter method with our single-pixel Echelle spectrometer system to create an efficient IR gas sensor.

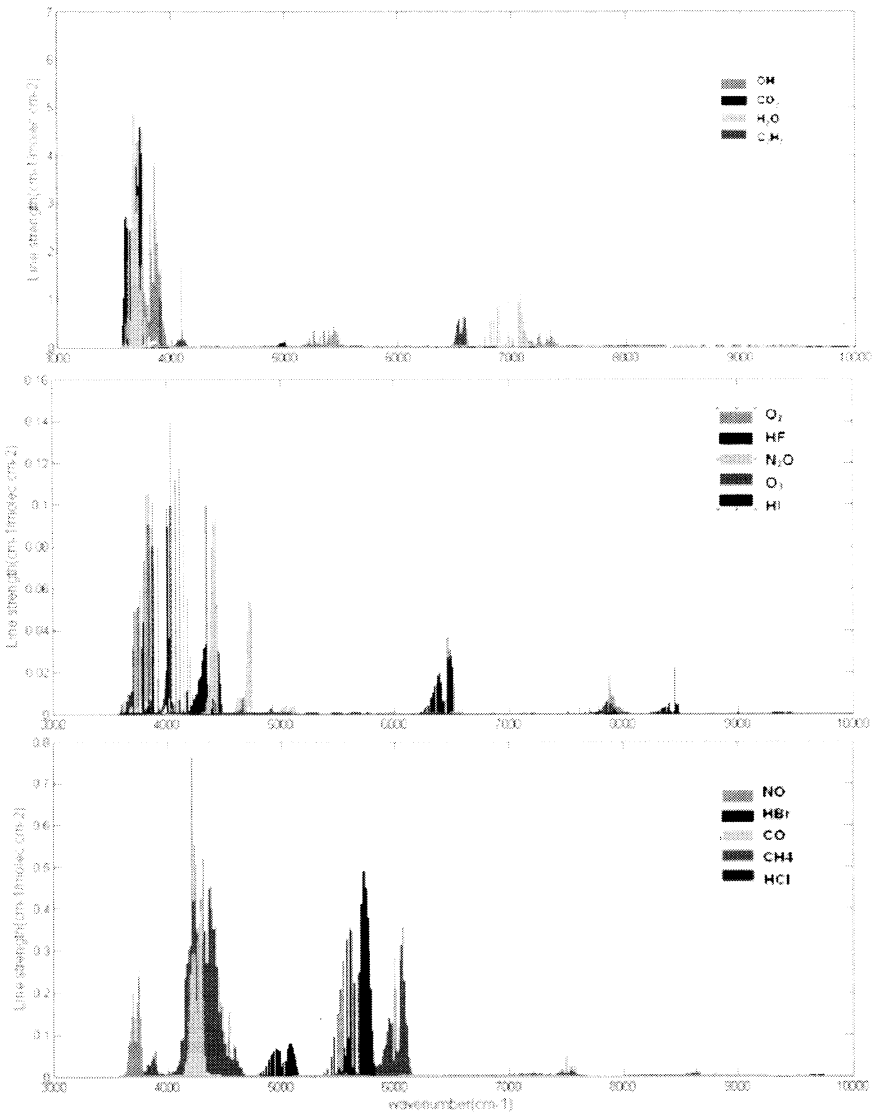

Figure 4.10 Plots of the absorption spectra of 14 different gases

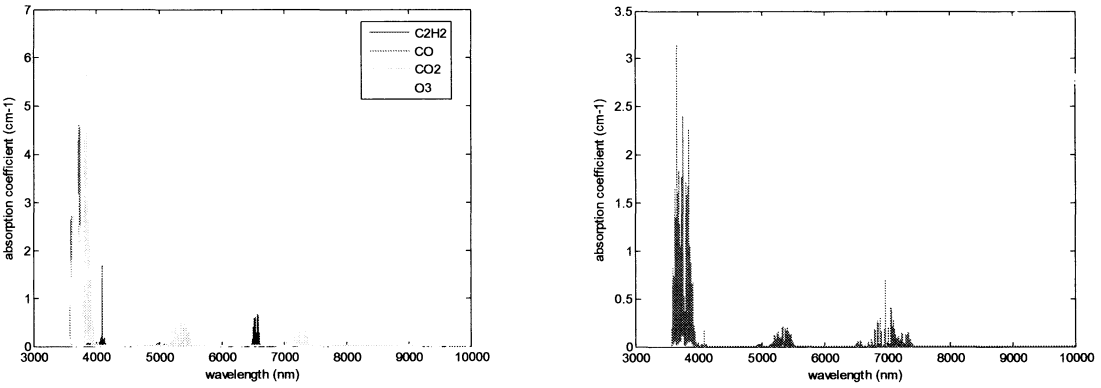

Figure 4.11 Individual spectra and the created composite spectrum of 4 gases

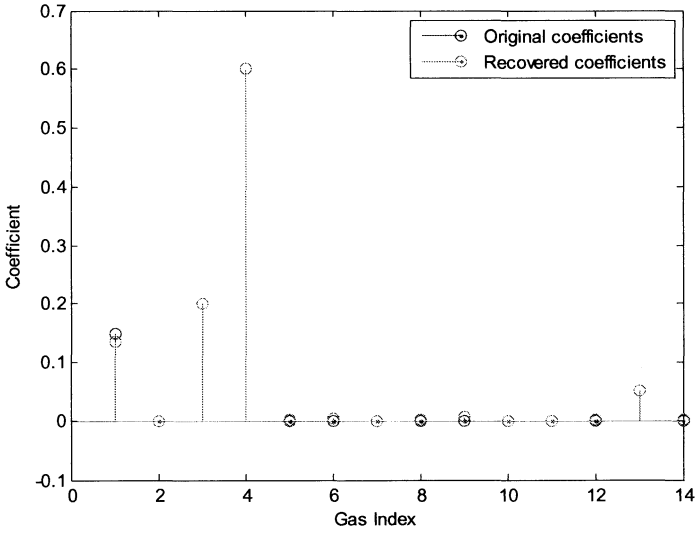

Figure 4.12 Noiseless, 6500 pixesl, recovered coefficients vs. original coefficients with 0.46% (30) measurements ($\sigma = 0.006$)

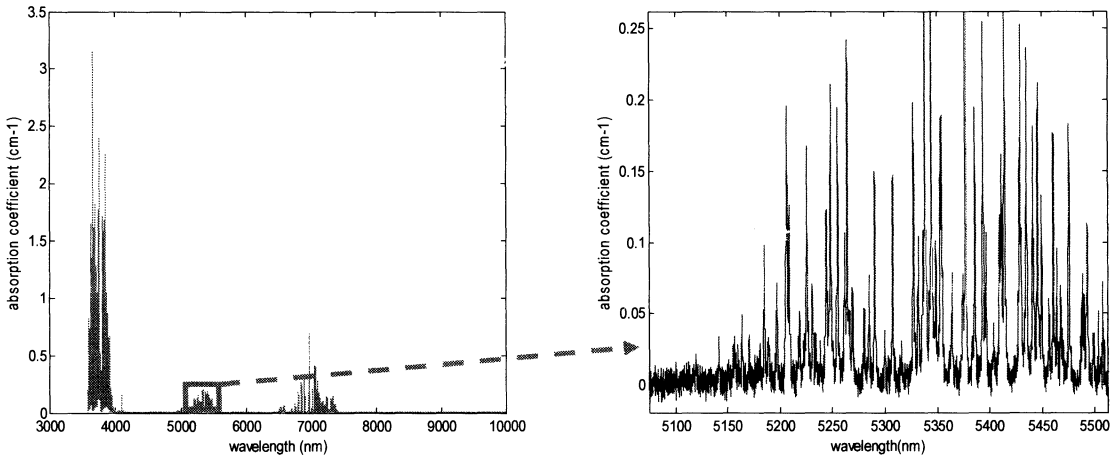

Figure 4.13 Test spectrum with the added noise

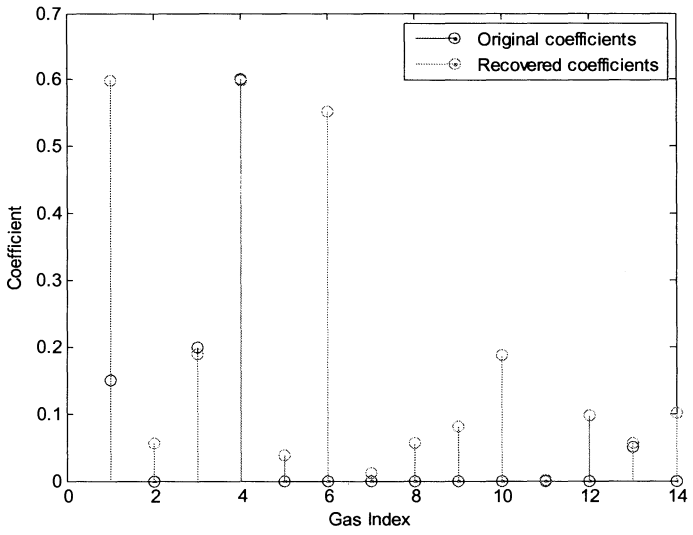

Figure 4.14 Noisy case, 256 pixels, recovered coefficients vs. original coefficients with 100% (256) measurements ($\sigma = 0.758$)

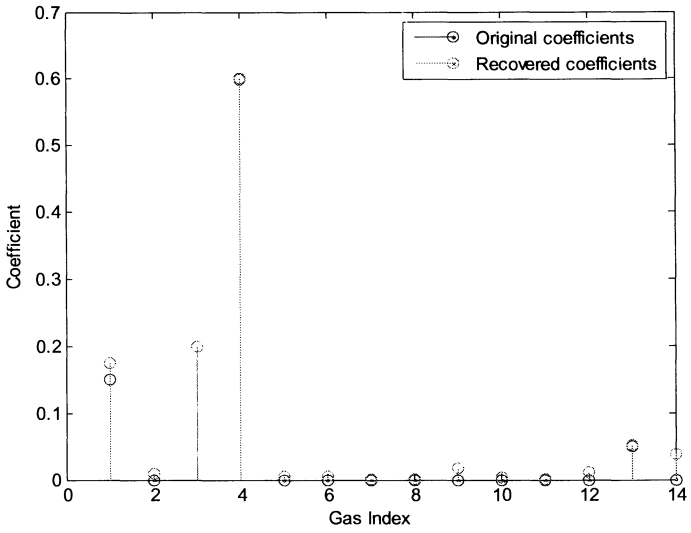

Figure 4.15 Noisy case, 6500 pixels, recovered coefficients vs. original coefficients with 3.93% (256) measurements ($\sigma = 0.055$)

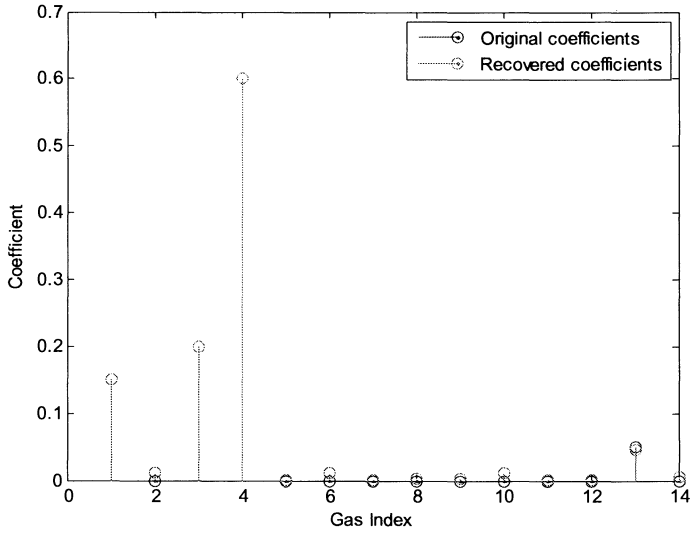

Figure 4.16 Noisy case, 6500 pixels, recovered coefficients vs. original coefficients with 6.15% (400) measurements ($\sigma = 0.022$)

References

1. Wikipedia, "Algorithmics of Sudoku — Wikipedia, The Free Encyclopedia," 2009 [Online; accessed 13-May-2009].
2. A. Bartlett and A. Langville, "An Integer Programming Model for the Sudoku Problem," *available at http://www.cofc.edu/~langvillea/Sudoku/sudoku2.pdf,* 2006
3. J. Sampsell, "An overview of the digital micromirror device (DMD) and its application to projection displays,"*SID Int. Symp. Digest of Technical Papers*, vol. 24, p. 1012, 1993
4. C. E. Shannon, "Communication in the presence of noise," *Proceedings of the IEEE*, vol. 86, NO. 2, 1998
5. E. J. Candµes and J. Romberg, "Sparsity and incoherence in compressive sampling," *Inverse Problems*, 23(3) pp. 969-985, 2007
6. D. L. Donoho, "Compressed sensing," *IEEE Trans. Info. Theory*, vol. 52, pp. 1289-1306, Sept. 2006.
7. W. Guo, W. Yin, "EdgeCS: edge guided compressive sensing reconstruction," *Proceedings of the SPIE*, vol. 7744, pp. 77440L-77440L-10, 2010
8. D. Donoho and M. Elad, "Optimally sparse representation in general (nonorthogonal) dictionaries vis ℓ1minimization," *Proceedings of the National Academy of Sciences 100*, pp. 2197–2202, 2003

9. D. Donoho and X. Huo, "Uncertainty principles and ideal atomic decompositions," *IEEE Transactions on Information Theory 47*, pp. 2845–2862, 2001

10. J. Fuchs, "On sparse representations in arbitrary redundant bases," *IEEE Transactions on Information Theory 50,* pp. 1341–1344, 2004.

11. L. Rudin, S. Osher and E. Fatemi, "Nonlinear total variation based on noise removal algorithms," *Phys. D*, vol. 60, p. 259-268, 1992

12. A. Chambolle and P. L. Lions, "Image recovery via total variation minimization and related problems," *Numer. Math.,* vol. 76, pp. 167–188, 1997.

13. T. F. Chan, S. Esedoglu, F. Park, and A. Yip, "Recent developments in total variation image restoration," *CAM Report 05-01, Department of Mathematics, UCLA,* 2004.

14. A. Chambolle, "An algorithm for total variation minimization and applications," *Journal of Mathematical Imaging and Vision,* vol. 20, 89–97, Jan. 2004.

15. C. Li, W. Yin, Y. Zhang, "TVAL3: TV minimization by Augmented Lagrangian and ALternating direction ALgorithms ," available at http://www.caam.rice.edu/~optimization/L1/TVAL3/

17. T. Beer, "Walsh Transforms," *American Journal of Physics,* vol. 49, NO. 5, May 1981

17. K.G. Beauchamp, "Applications of Walsh and Related Functions," *Academic Press,* 1984

18. D. J. Schroeder, "Echelle Efficiencies: Theory and Experiment; Author's Reply to Comment," *Appl. Opt.* vol. 20, NO. 4, p. 530-531, 1981

19. F. H. Chaffee, Jr, D. J. Schroeder, "Astronomical Applications of Echelle Spectroscopy," *Annual Review of Astronomy and Astrophysics*, vol. 14, p. 23-42, 1976

20. D. J. Schroeder, "Design Considerations for Astronomical Echelle Spectrographs," *Publications of the Astronomical Society of the Pacific,* Vol. 82, No. 490, p.1253, 1970

21. D. J. Schroeder, C. M. Anderson, "Echelle Spectrograph for Astronomical Use," *Pub. Astron. Soc. Pacific,* vol. 83, August 1971

22. M. A. Davenport, M. F. Duarte, M. B. Wakin, J. N. Laskar, D. Takhar, K. F. Kelly, R. G. Baraniuk, "The Smashed Filter for Compressive Classification and Target Recognition," *Proc. of Computational Imaging V at SPIE Electronic Imaging,* January 2007

23. E. van den Berg, M. P. Friedlander, "Sparse optimization with least-squares constraints," *Tech. Rep. TR-2010-02,* January 2010

24. E. van den Berg, M. P. Friedlander, "Probing the Pareto Frontier for Basis Pursuit Solutions," *SIAM J. SCI. COMPUT.,* vol. 31, No. 2, pp. 890–912, 2008